Climate Dynamics (2020) 54:3879–3905
https://doi.org/10.1007/s00382-020-05204-7

The April 2010 North African heatwave: when the water vapor greenhouse effect drives nighttime temperatures

Yann Largeron[1] · Françoise Guichard[1] · Romain Roehrig[1] · Fleur Couvreux[1] · Jessica Barbier[1]

Received: 28 March 2019 / Accepted: 5 March 2020 / Published online: 6 May 2020

Abstract

North Africa experienced a severe heatwave in April 2010 with daily maximum temperatures (T_{max}) frequently exceeding 40 °C and daily minimum temperatures (T_{min}) over 27 °C for more than five consecutive days in extended Saharan and Sahelian areas. Observations show that areas and periods affected by the heatwave correspond to strong positive anomalies of surface incoming longwave fluxes (LW_{in}) and negative anomalies of incoming shortwave fluxes (SW_{in}). The latter are explained by clouds in the Sahara, and by both clouds and dust loadings in the Sahel. However, the strong positive anomalies of LW_{in} are hardly related to cloud or aerosol radiative effects. An analysis based on climate-model simulations (CNRM-AM) complemented by a specially-designed conceptual soil-atmospheric surface layer model (SARAWI) shows that this positive anomaly of LW_{in} is mainly due to a water vapor greenhouse effect. SARAWI, which represents the two processes driving temperatures, namely turbulence and longwave radiative transfer between the soil and the atmospheric surface layer, points to the crucial impact of synoptic low-level advection of water vapor on T_{min}. By increasing the atmospheric infrared emissivity, the advected water vapor dramatically increases the nocturnal radiative warming of the soil surface, then in turn reducing the nocturnal cooling of the atmospheric surface layer, which remains warm throughout the night. Over Western Sahel, this advection is related to an early northward incursion of the monsoon flow. Over Sahara, the anomalously high precipitable water is due to a tropical plume event. Both observations and simulations support this major influence of the low-level water vapor radiative effect on T_{min} during this spring heatwave.

Keywords Heatwave · Radiative physics · Greenhouse effect · North Africa

1 Introduction

Heatwaves and their impacts over Europe or Western countries have been widely studied (e.g. Beniston 2004; Black et al. 2004; Perkins 2015 for a review). They received much less attention elsewhere, especially in North Africa. However, climate projections indicate that North Africa, where climate is among the warmest and driest on Earth, will be particularly affected by climate changes in a near future (Roehrig et al. 2013; Deme et al. 2017). Furthermore, heatwaves have become more frequent and severe in the past three decades (Fontaine et al. 2013; Moron et al. 2016) and these trends are projected to continue (IPCC 2013). This could become an exacerbating factor of vulnerability of North African societies whose adaptation strategies appear limited, due to their low hydrological resources and agricultural productivity (IPCC 2014; Sultan and Gaetani 2016).

In the Sahel, springtime has exhibited a strong trend of climate warming since 1950 (Guichard et al. 2012, 2017), up to twice the corresponding trend observed over Europe. This strong warming more significantly occurs during the hottest months of the year (April, May), at the end of the dry season, before the onset of the West African monsoon. This combination leads to heatwaves of unprecedented strong magnitude, an example of which occurred in spring 2010, where temperature peaks higher than 45 °C were recorded in many Sahelian countries (Niger, Senegal, Mali, Burkina Faso and Chad). These very high temperatures had strong impacts on morbidity and mortality (e.g. Honda et al. 2014).

Progressive multi-day soil desiccation has been recently pointed out as a major process operating during mid-latitude mega-heatwaves, like those who took place in Europe in 2003 or in Russia in 2010 (Miralles et al. 2014; Fischer

✉ Yann Largeron
ylargeron@gmail.com

[1] CNRM, Université de Toulouse, Météo-France, CNRS, Toulouse, France

2014). However, this process is unlikely to operate over North Africa during springtime since soils are mostly dry at this period of the year and remain so until the arrival of the monsoon rain (e.g. Baup et al. 2007). In contrast, Sahelian heatwaves appear to be frequently associated with an increase of moisture (Guichard et al. 2009 and further evidences in the present study). Physical mechanisms operating during these heatwaves therefore still need to be identified.

Using in-situ observations in the central Sahel, Guichard et al. (2009) show that nighttime minimum temperatures increase by several degrees during the first incursions of the moist monsoon flow in spring, while the incoming longwave flux at the surface varies accordingly. Therefore, couplings between surface air temperature, humidity and radiative fluxes are expected, particularly during nighttime. On the other hand, springtime in the Sahel is often associated with high dust loadings (Brooks and Legrand 2000; Basart et al. 2009; Klose et al. 2010), mid-level clouds and cirrus. These processes are likely to limit daytime incoming fluxes, boundary layer growth and therefore daytime warming. These contrasting impacts on low-levels suggest a strong diurnal cycle of the physical processes acting during springtime heatwaves, implying reduced daytime warming and reduced nighttime cooling with partly compensating effects on daily-average temperatures in unknown proportions.

Over the Sahel and Sahara, the surface and Top Of Atmosphere (TOA) energy budget is affected by aerosols, that are known to have a radiative impact both in the longwave and shortwave bands, generally leading to a negative net effect (Balkanski et al. 2007). Similarly, cloud cover induces a longwave warming generally overcompensated by a shortwave cooling (Bouniol et al. 2012). Recently, Marsham et al. (2016) studied the respective impacts of water vapor and dust aerosols in controlling the radiative budget over the Sahara, using both in-situ observations and satellite retrievals. They concluded that the total column water vapor provides a stronger control on TOA net radiative fluxes than the aerosols. However, they also noted that dust loadings are correlated to water vapor, so that their methodology can not disentangle the relative effect of each other.

Identifying the physical mechanisms at play in North Africa during springtime, and especially during heatwaves; describing their diurnal cycle evolution; their impact on the surface energy budget and the near surface temperature therefore still need to be done. The present study aims at filling these gaps, with a particular focus on the major heatwave of April 2010. In line with these objectives, we will also present a new approach making use of a specially-designed conceptual model that allows to isolate the radiative impact of water vapor alone and therefore directly quantifies its impact on the energy budget, distinctly from the effects of aerosols and clouds.

This study shows that the 2010 heatwave is characterized by strong positive anomalies of daily-minimum temperatures and the incoming longwave fluxes over North Africa by making use of several long-term observational datasets (satellite-based products and ground-stations, described in Sect. 2). It further explores the radiative impacts of clouds and aerosols on 2-m temperatures (Sects. 3 and 4) and shows that, although strong positive anomalies of AOD and cloud cover are found respectively over the Sahel and Sahara, their radiative impacts are too weak to explain the anomalies of longwave fluxes and temperatures. Boundary-layer physics is further explored with climate simulations performed with the atmospheric component of the Centre National de Recherches Météorologiques (CNRM) climate model, using a configuration in which the dynamics is nudged towards a reanalysis (Sect. 5). It shows that turbulence in the atmospheric surface layer and longwave radiation are the main drivers of the evolution of 2-m temperatures during the heatwave and that the longwave radiative coupling between the soil and the air surface layer is strongly affected by the infrared emissivity of the atmosphere, which is in turn strongly related to the 2-m specific humidity. Finally, a new and specially designed prognostic model of surface-atmosphere radiative exchanges (hereafter called SARAWI) is presented. This model is used to explore and quantify the impact of the radiative greenhouse effect of water vapor on surface air temperature (Sect. 6), and we introduce a Humidity Radiative Effect (hereafter HRE) based on the model estimates. It shows that the heatwave is controlled by the anomalously high specific humidity related to an early monsoon flux intrusion into the Sahel, and to a coincident tropical plume into the Sahara. Conclusions are given in the final section.

2 Data and methods

2.1 Surface temperature databases

This study makes use of the Berkeley Earth Surface Temperature gridded dataset, hereafter referred to as BEST. This product uses the statistical Kriging method to interpolate data from ground-based stations on a global regular $1° \times 1°$ grid (Rohde et al. 2013). The dataset uses 2-m temperatures from an ensemble of weather stations compiled from 16 preexisting data archives, among which the Global Historical Climatology Network (GHCN), and further compiles data over 39,000 ground-stations.

In the following, we use daily-minimum, daily-maximum and daily-average temperatures T_{min}, T_{max} and T_{avg} which are available from 1880 to 2013, at a daily time scale.

For each grid point, we compute daily climatological values over the 2000–2013 period (by averaging values for the 14 years and using a 21-day running mean) for T_{min}, T_{max} and

T_{avg}. Hereafter, daily anomalies for 2010 are estimated from this 2000–2013 climatology (this relatively short period, 2000–2013, was chosen for consistency with the analysis of the satellite data presented below). We also compute, at each grid point, the daily 90% quantile values of the temperature distributions built with the $21 \times 14 = 294$ values of the 21 calendar days centered on the considered day and the 14 years of the 2000–2013 period.

We also used data from 222 SYNOP ground stations across North Africa archived by the French weather service Météo-France.

2.2 The Clouds and the Earth's Radiant Energy System (CERES) database

We also use data from the Clouds and the Earth's Radiant Energy System (CERES) database, developed by NASA (Wielicki et al. 1996, 1998), which are available from 2000 to 2017. We use the SYN1deg dataset, which is a level 3 satellite product which provides CERES-observed radiative fluxes at 3-hourly and daily temporal resolution on a $1° \times 1°$ grid, together with coincident Moderate Resolution Imaging Spectroradiometer (MODIS)-derived cloud and aerosol properties, and geostationary-derived cloud properties and broadband fluxes that have been carefully normalized with CERES fluxes. The use of measurements from a constellation of geostationary orbiting satellites allows to more accurately model the variability between CERES Terra and Aqua satellite observations (cf. Doelling et al. 2013 for a description of the methodology). This dataset also provides daily average $1° \times 1°$ gridded data of cloud cover, total Aerosol Optical Depth at 0.55 µm (hereafter AOD), and total column Precipitable Water (hereafter PW) estimated by MODIS.

We also use the Earth's surface computed upwelling and incoming shortwave (hereafter SW_{in} and SW_{up}) and longwave (LW_{in} and LW_{up}) fluxes, for all-sky, clear-sky (cloud free) and pristine (cloud and aerosol free, hereafter referred to as clean-sky) conditions. Surface fluxes are provided with a 3-h timestep using a radiative transfer code (Fu and Liou 1992) based upon inputs from Terra and Aqua MODIS and 3-hourly geostationary data (for cloud and aerosol properties), and meteorological assimilation data from the Goddard Earth Observing System Model reanalyses (for meteorological profiles). Several sources of uncertainties arise in these estimations of the daily surface fluxes. Rutan et al. (2015) evaluated them using 8 years of in-situ observations and concluded that downward fluxes have a bias of 3.0 W m^{-2} in the shortwave and – 4.0 W m^{-2} in the longwave. Results of the present study are given within these uncertainties.

We compute local daily climatological values for all these fields over 2000–2013 in the same way as done for BEST temperatures.

2.3 Automatic weather stations observations in the Sahelian Gourma (AMMA-CATCH)

The present study also uses ground-station measurements made in the Sahelian Gourma (Mali), deployed at a site which belongs to the African Monsoon Multi-disciplinary Analysis (AMMA)-CATCH network (Mougin et al. 2009).

In the following, we mostly focus on the measurement site of Agoufou, located in central Sahel, at 15°20′40″ N and 1°28′45″ W. Instruments are deployed in grassland, over sandy soil, which is the dominant surface type in the Malian Gourma. An automatic weather station (AWS) acquires data at a 15-min time step since April 2002, and provides air temperature, relative humidity, rainfall, wind speed and direction as well as surface radiative and turbulent fluxes.

The site is homogeneous over several kilometers, which allows a good estimate of the radiative fluxes. These data have already been used for thermodynamic and climate analyses by Guichard et al. (2009), Timouk et al. (2009), Roehrig et al. (2013) and Lohou et al. (2014) among others.

2.4 CNRM-AM nudged simulation

In the present study, we use a simulation based on the atmospheric component of a prototype of the new CNRM climate model, hereafter referred to as CNRM-AM. This model is based on the version 6.2.1 of the ARPEGE-Climat atmospheric model (Déqué et al. 1994; Voldoire et al. 2013) and benefits from several significant and recently-implemented developments of the model physics parameterizations. This prototype version is similar to that used in the recent studies of Michou et al. (2015), Leroux et al. (2016), Martin et al. (2017).

CNRM-AM is a major update of the CNRM-CM5 atmospheric component (Voldoire et al. 2013). It contains a prognostic turbulent kinetic energy (TKE) scheme (Cuxart et al. 2000) that improves the representation of the dry boundary layer. The new convection scheme represents in a unified way the dry, shallow and deep convective regimes, following Guérémy (2011) and Piriou et al. (2007). The convection scheme microphysics prognostically describes cloud liquid and ice water, as well as rain and snow specific masses following the work of Lopez (2002). It is also fully consistent with the microphysics scheme used for the large-scale condensation and precipitation. Cloud macrophysics is handled by the Ricard and Royer (1993) scheme. The radiation scheme is based on the shortwave scheme of Fouquart and Bonnel (1980) and on the longwave Rapid Radiation Transfer Model (RRTM, Mlawer et al. 1997). An overview of the land surface model SURFEX can be found in Masson et al. (2013) and more details on the physical content used in the present study is described in Decharme et al. (2013, 2016).

SURFEX makes use of the ECOCLIMAP database for surface parameters (Masson et al. 2003).

CNRM-AM is a spectral model that has been used here with a T127 truncation (about 1.4° resolution at the Equator). It has 91 vertical hybrid levels up to 80 km. The first model level is near 12 m and the model has about 10 levels in the first atmospheric kilometer. It is run in an Atmospheric Model Intercomparison Project (AMIP) configuration, in which monthly-mean sea surface temperatures are prescribed and interpolated at each time step of the model (equal to 15 min). Monthly aerosol loadings are also prescribed and constant across each month. A climatological annual cycle is used, which is computed from the 1990–1999 period of a nudged AMIP simulation of CNRM-AM with the prognostic aerosol scheme described in Michou et al. (2015). Note that aerosol optical properties were updated according to Nabat et al. (2013), compared to those used in CNRM-CM5.

Here, the main objective is to analyze the effects of the physical processes during the April 2010 Sahelian heatwave, without the additional complexity induced by their interactions with the large-scale dynamics. Therefore, a dynamical spectral nudging towards the 6-hourly ERA-interim reanalyzed fields (Dee et al. 2011) is applied to the wind vorticity and divergence as well as to the surface pressure, which constrains the model to follow the observed large-scale dynamical sequence (Coindreau et al. 2007). The relaxation timescale is 12 h for the vorticity and 24h for the divergence and surface pressure. To let the model physics adjusts in the surface layer, the nudging is weakened at the first four model levels (approximately up to 400 m above the ground), with no nudging at all at the first model level. Note also that the simulation started on 1 January 1979 and ended on 31 December 2012, so that the atmospheric and land-surface model spin-up can be neglected when focusing on April 2010.

2.5 A conceptual prognostic model: the Surface-Atmosphere RAdiative Water vapor Impact (SARAWI) model

A conceptual prognostic model has been specifically designed: the Surface-Atmosphere RAdiative Water vapor Impact model (SARAWI). It is used in this study to investigate the processes involved in the temperature fluctuations.

This conceptual model appears to be a useful tool to:

- Highlight the influence of physical processes. Hereafter, the impact of the water vapor greenhouse effect is investigated, and the model allows to infer a Humidity Radiative Effect (cf Sects. 6.3 to 6.5);
- Provide a simple-way to test the ability of new formulations of the physical processes to correctly reproduce observations. For instance, hereafter, a linear regression of the air emissivity is proposed in Eq. (9) and evaluated in Sect. 6.1.
- Point out the biases and sources of uncertainty in state-of-the-art models and parameterizations (hereafter, when compared to the CNRM-AM model and observations, cf. Sects. 6.1, 6.2)
- Perform and interpret sensitivity tests in simple and unambiguous ways for a low computational cost, contrary to complex GCM simulations (hereafter by modifying only the longwave radiative effect of low-level humidity, cf. Sects. 6.3, 6.4).

2.5.1 Basic concepts and hypotheses

SARAWI consists of a simple model of the soil and lower atmosphere. It aims at investigating the interactions at play between physical processes and the impact of their parameterizations on the evolution of the soil surface temperature T_s and of the surface-layer air temperature T_a.

SARAWI assumes that turbulence and radiative transfer are the dominant terms explaining the evolution of T_s and T_a. The model solves local physical processes acting in the boundary-layer (turbulence and radiation transfer) by decoupling them from the regional and synoptic atmospheric processes that are either prescribed analytically or solved by an external GCM-type model and prescribed into the SARAWI model. As shown in Sects. 5 and 6, these hypotheses are supported by the results given by the CNRM-AM simulation, and our results suggest that this approach is sufficient to reproduce the spatial structure and temporal evolution of the 2-m air temperature T_{2m}, at least over North Africa during springtime 2010. The model can therefore be used to analyze the relative contributions of regional-scale circulations versus local-scale processes.

In the SARAWI model, the soil and lower atmosphere are represented with two soil layers and one atmospheric layer, with the mass point of the atmospheric layer located at $\delta z/2$ above the ground, δz being the atmospheric layer depth. It can be used in a one dimensional (1D) mode at a selected location, or over a given domain (hereafter all North Africa), as a light 3D model, with vertical transfers only, explicitly represented across its three layers.

SARAWI solves three prognostic equations (one for the temperatures of each of the three layers), together with a diagnostic equation for T_{2m} (details are given below). It makes use of four additional equations for the physical parameterization of fluxes and tendencies, combined with ten tuned or statistically-fitted parameterizations that account for physical properties. Finally, simulations are performed with four external input fields.

2.5.2 SARAWI system of equations and parameterizations

Inputs SARAWI makes use of four input fields, that can be prescribed analytically or from an atmospheric model. They are indicated in the "Inputs" field in Table 1.

Prognostic equations SARAWI solves three prognostic equations for T_a, T_s and T_{2s} respectively the temperatures of the atmospheric layer, the soil surface layer and the deep soil layer. They are detailed in the "Pronostic equations" field of Table 1. The different terms on the right hand sides are detailed in the "Physical parameterizations" field.

Equation (1) is the classical thermodynamic equation in which we make the assumption that the effects of shortwave radiation, parameterized convection, large-scale condensation and precipitation, and advection are negligible in the atmospheric surface layer, so that the evolution of air surface temperature is mainly driven by longwave radiation and turbulence. We will show in Sect. 5 that this hypothesis is supported by climate-model simulations.

Equations (2) and (3) follows a simple parameterization for a two-layers soil model, using the classical force-restore method of Noilhan and Planton (1989).

The last term on the right-hand side of Eq. (2) is proportional to a diffusive heat flux into the deep soil layer and tends to restore T_s to the mean soil temperature T_{2s}. C_s is the inverse of the soil heat capacity. In Eq. (2), the latent heat flux is assumed to be negligible, which is a realistic assumption over the Sahel and Sahara at the end of the dry season (cf. Sect. 5). Equations (2) and (3) introduce a relaxation time constant (τ) fixed at $\tau = 24$ h, as in Noilhan and Planton (1989).

Physical parameterizations Four physical parameterizations are used (cf. Eqs. (4)–(7) in Table 1). All parameters and variables present in Eqs. (4)–(7) are detailed in Table 2.

Equations (4) and (5) correspond to classical formulations of the sensible heat flux and the net longwave flux at the surface (e.g. Noilhan and Planton 1989).

The longwave radiation warming of the atmospheric layer is given by Eq. (6), which is a simplification of the longwave model of Mlawer et al. (1997) corresponding to a radiative balance within the atmospheric layer. Its first term corresponds to the infrared absorption by the atmospheric layer of the emitted infrared flux from the surface, and its second corresponds to the emitted infrared flux toward the surface combined with the absorbed part of that same flux reflected over the soil surface. The coefficient h_{rad} is a radiative scale height (see Table 2 and Sect. 2.5.3), which represents the height of the layer radiatively affected by the surface, in the sense that the upwelling longwave at the surface LW_{up} is absorbed within the layer of height h_{rad}, and respectively that no longwave radiation emitted from above that layer reaches

Table 1 The system of equations and parameterizations of the SARAWI pronostic model

Inputs		
(a)	SW_{net}	Net shortwave flux at the surface
(b)	hus	Specific humidity at the atmospheric level
(c)	V_a	Wind speed at the atmospheric level
(d)	T_{2a}	Temperature of the air above the SARAWI atmospheric layer (used in the parameterization of turbulence only)
Pronostic equations		
(1)	$\frac{\partial T_a}{\partial t} = \frac{\partial T_a}{\partial t}_{rlw} + \frac{\partial T_a}{\partial t}_{pbl}$	Atmospheric layer temperature (T_a) equation
(2)	$\frac{\partial T_s}{\partial t} = C_s \cdot (SW_{net} + LW_{net} - H) - \frac{2\pi}{\tau}(T_s - T_{2s})$	Soil surface layer temperature (T_s) equation
(3)	$\frac{\partial T_{2s}}{\partial t} = \frac{1}{\tau}(T_s - T_{2s})$	Deep soil layer temperature (T_{2s}) equation
Physical parameterizations		
(4)	$H = \rho \cdot C_p \cdot C_h \cdot V_a \cdot (T_s - T_a)$	Surface sensible heat flux parameterization
(5)	$LW_{net} = \sigma \cdot (\epsilon_a \cdot T_a^4 - \epsilon_s \cdot T_s^4)$	Surface net longwave flux parameterization
(6)	$\frac{\partial T_a}{\partial t}_{rlw} = \frac{\sigma}{\rho \cdot C_p \cdot h_{rad}} \cdot \{\epsilon_a \cdot \epsilon_s \cdot T_s^4 - [1 - \epsilon_a(1 - \epsilon_s)] \cdot \epsilon_a \cdot T_a^4\}$	Longwave tendency parameterization
(7)	$\frac{\partial T_a}{\partial t}_{pbl} = K_s \frac{V_a(T_s - T_a)}{\delta z} + K_h \frac{T_{2a} - T_a}{\delta z \cdot h_{turb}}$	Turbulent tendency parameterization
Diagnostic equations		
(8)	$T_{2m} = T_s + c_{t2m} \cdot T_a$	2-m air temperature diagnostic

Table 2 The physiographic and physical parameters used by the SARAWI pronostic

Variable	Description	Fixed value or parameterization used
ρ	Air density	$\rho = 1.2$ kg m^{-3}
C_p	Air specific heat capacity	$C_p = 1004$ J kg^{-1} K^{-1}
σ	Stefan–Boltzman constant	$\sigma = 5.67 \times 10^{-8}$ W m^{-2} K^{-4}
τ	Relaxation time constant	$\tau = 24$ h (Force-restore approach of Noilhan and Planton (1989))
ϵ_s	Soil surface total infrared emissivity	$\epsilon_s = 0.9946$ North African average, extracted from the ECOCLIMAP database (Champeaux et al. 2005; Faroux et al. 2013)
ϵ_a	Air total infrared emissivity	$\epsilon_a = a_1 + a_2 \cdot hus + a_3 \cdot T_a$ $a_1 = 0.667$, $a_2 = 1.17 \times 10^{-2}$ with hus in g/kg and $a_3 = 4.55 \times 10^{-4}$ with T_a in °C
C_s	Inverse of the soil heat capacity	Extracted from the ECOCLIMAP database (Champeaux et al. 2005; Faroux et al. 2013) Averaged over daytime and nighttime: $C_s^{night}(lon, lat)$ and $C_s^{day}(lon, lat)$
h_{rad}	Radiative scale height	$h_{rad} = c_{rad} \cdot \delta z$, with $c_{rad} = 4.74$
h_{turb}	Turbulent scale height	$h_{turb} = \delta z_2 = 35$ m
C_h	Drag coefficient	Daytime $C_h = 4 \times 10^{-3}$. Nighttime: $C_h = 5 \times 10^{-4}$
K_s	Turbulent drag coefficient	Daytime: $K_s = 1.6 \times 10^{-4}$. Nighttime: $K_s = 2 \times 10^{-5}$
K_h	Turbulent diffusivity	Daytime: $K_h = 0.94$ m^2 s^{-1}. Nighttime: $K_h = 0.08$ m^2 s^{-1}
c_{t2m}	Static stability dependent coefficient	Based on Mahfouf et al. (1995)

More details are given in "Appendix"

the soil surface without being absorbed. The introduction of h_{rad} in Eq. (6) makes explicit that the transmitted incoming longwave radiation at the surface issued from above the altitude h_{rad} can be neglected.

The turbulent processes are parameterized with Eq. (7), which is a simplification of the Mellor and Yamada (1982) turbulence scheme for a one-layer atmospheric model. The first term corresponds to a turbulent exchange with the soil surface layer and the second to a turbulent exchange with the air above the atmospheric layer.

Diagnostic equation for T_{2m} The 2-m air temperature T_{2m} is diagnosed with a linear interpolation between the soil surface temperature T_s and the air layer temperature T_a, given by Eq. (8), as usual in atmospheric model. The coefficient c_{t2m} typically depends on the static stability of the atmosphere. Here, we parameterize this coefficient according to Mahfouf et al. (1995).

2.5.3 Physiographic and physical parameters

In Eqs. (3)–(8), ten parameters have to be tuned, prescribed or parameterized: τ, ϵ_s, ϵ_a, C_s, h_{rad}, h_{turb}, C_h, K_s, K_h and c_{t2m}.

Among those parameters, ϵ_s and C_s are local physiographic properties dependent on ground cover and soil texture. They have to be prescribed using soil surface characteristics databases. C_s has a major importance since it strongly modulates the diurnal soil and air temperature ranges. ϵ_s is typically very close to 1.

h_{rad}, h_{turb}, C_h, K_s and K_h have to be tuned or statistically fitted, and c_{t2m} requires a parameterization.

For ϵ_a, we propose an original and simple approach. While longwave radiative fluxes directly depends on temperature through the Stefan–Boltzman's law, longwave emissivity ϵ_a (and fluxes) also varies with atmospheric water vapor (e.g. Prata 1996). Since the SARAWI model has been mainly designed (and will be used hereafter) to evaluate the radiative impacts of water vapor, it appears crucial that the parameterized infrared emissivity be sensitive to its variations. Similarly to Herrero and Polo (2012), we propose a simple parameterization based on a multiple linear regression:

$$\epsilon_a = a_1 + a_2 \cdot hus + a_3 \cdot T_a \tag{9}$$

Table 2 synthesized the fixed values or parameterizations used in the SARAWI model. Note that this could be easily modified in other versions of the model in order to improve some representations of these parameters or to adjust them to other areas of the globe.

"Appendix" gives details on the reasons for using values and parameterizations given in Table 2, the methodology used to infer those values and some uncertainties as compared to other parameterizations.

2.5.4 Configuration of the SARAWI simulations

In the present study, SARAWI simulations are made for April 2010 over North Africa, between 0° and 30° N in latitude and between 20° W and 20° E in longitude. The depth of the atmospheric layer is $\delta z = 25$ m, the horizontal resolution is fixed to $1.4° \times 1.4°$ and the time step is 15-min, in order to compare results to CNRM-AM simulations.

The simulations are initialized using T_a and T_s from the CNRM-AM simulation on 1st April; and T_{2s} is assumed to be equal to T_s at the first time step (in practice, after the spin-up period, which lasts less than 24 h, the precise choice of the initial field of T_{2s} has no influence on our results).

3 Observed large-scale features on spring 2010

In this section, we make use of the previously described long-term observational datasets to show that the 2010 heatwave is characterized by strong positive anomalies of the daily-minimum temperatures and the incoming longwave fluxes over North Africa, correlated with positive anomalies of precipitable water.

3.1 Maps of April 2010 anomalies

In the present study, we refer to "North Africa" to describe the geographic region of Africa located between 0° N and 30° N; 20° W and 20° E. Hereafter, two subregions of interest are defined: the Sahel, as the area between 14° N and 18° N; and the Sahara, between 18° and 30° N. Both of these subregions extend from 20° W to 20° E.

Figure 1 shows April 2010 monthly means and monthly anomalies of BEST T_{min} and T_{max}, CERES LW_{in}, SW_{in}, cloud cover fraction, AOD and PW.

In April 2010, T_{min} and T_{max} exhibit a springtime pattern with a maximum temperatures latitudinal band centered on the Sahel (see Fig. 1a). Similarly, the maximum of LW_{in} is localized over the Sahel. SW_{in}, cloud cover and PW exhibit distinct patterns characterized by strong meridional gradients. This highlights the contrast between the Sudano-Guinean region (south to 14° N) affected by the moist monsoon flow associated with clouds and reduced SW_{in}; and the Sahel and the Sahara subregions (see Fig. 1a) with stronger SW_{in}, reduced cloud cover and enhanced dryness (low PW). The AOD pattern emphasizes a maximum over Mali, Niger and South Algeria, which are dominantly affected by dust events due to the combination of strong winds, low surface roughness, dry soils and sporadic vegetation in springtime.

Strong positive temperature anomalies (up to 3 or 4 °C) are observed in the Sahel and Sahara, particularly strong over Mauritania, Algeria and Mali. T_{min} anomalies are

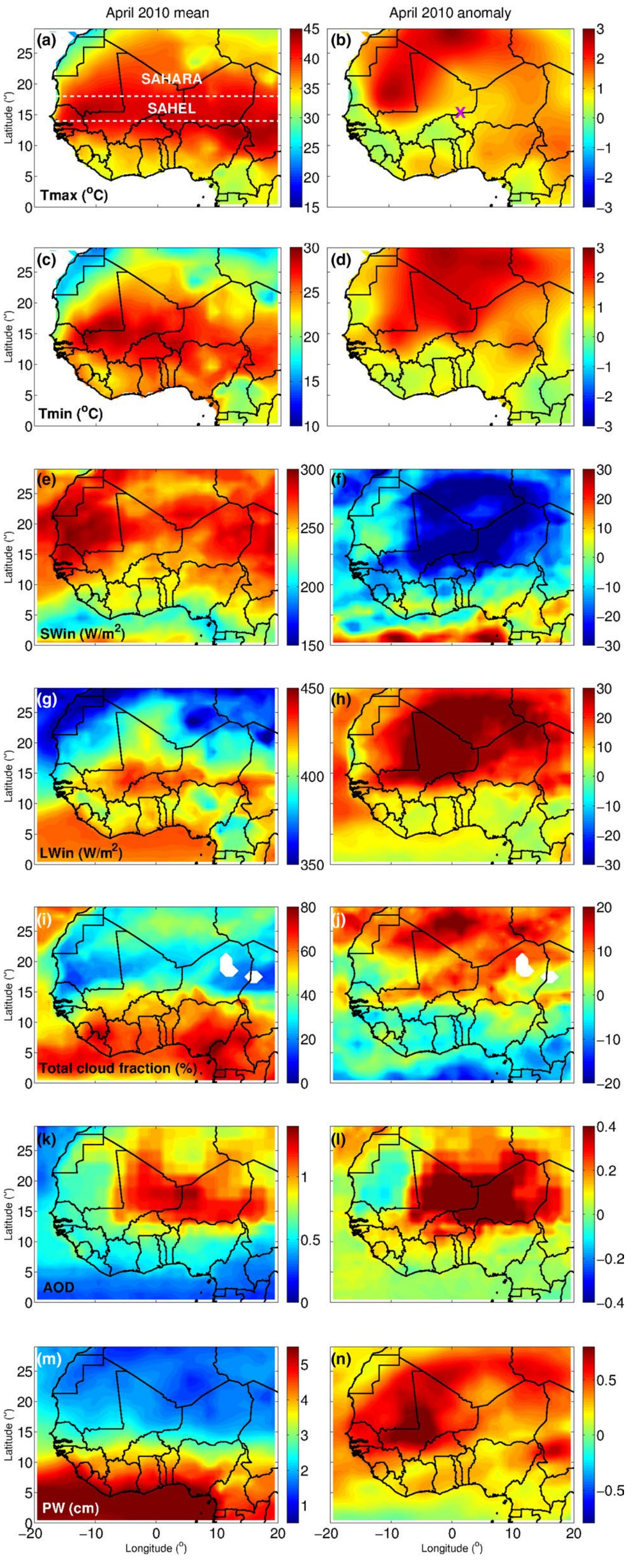

Fig. 1 Monthly-mean (left) and climatological anomalies (right) for April 2010 of T_{max} (**a**, **b**), T_{min} (**c**, **d**), SW_{in} (**e**, **f**) and LW_{in} (**g**, **h**) total cloud cover fraction (**i**, **j**), Aerosol Optical Depth (**k**, **l**) and Precipitable Water (**m**, **n**). White dotted lines in **a** delimitates Sahel and Sahara as defined in this study. Purple cross in **b** shows the location of the Agoufou station

stronger and impact a wide area, covering the western and central Sahel and Sahara (Fig. 1b, d). These regions correspond to enhanced LW_{in} in April 2010, strong compared to the climatology, reaching anomalies of about 30–40 W/m^2 (Fig. 1h). A strong negative SW_{in} anomaly is also observed in the Sahel and Sahara, with a similar pattern to that of the LW_{in} positive anomaly (Fig. 1f).

Strong positive anomalies of cloud cover, AOD and PW also occur over the Sahel and Sahara in April 2010 (Fig. 1j, l, n). The cloud cover increase mainly concerns the northern Sahara and is mostly related to enhanced high-level clouds (not shown). These anomalies are due to a tropical plume event, common in North Africa during spring (Knippertz and Martin 2005; Fröhlich et al. 2013). The tropical plume enhanced PW over Mauritania, Algeria and Libya and favored the occurrence of high clouds and low-level water vapor. PW is also increased over Mali and Burkina Faso, as the monsoon flow is anomalously north during this period. Strong AOD anomalies are located over Mali and Niger and are caused by several dust events.

3.2 Climatological and 2010 springtime evolution

In the following, two main climatological areas are considered: The Sahara and the Sahel, defined in the previous section. They both extend over the longitude band [20° W, 20° E] and only account for land pixels (Fig. 1a).

Figure 2a, b presents the climatological and 2010 time series of T_{min}, T_{avg} and T_{max} given by BEST and averaged over each of these two areas. The 2010 springtime (March–April–May) exhibits relatively strong positive temperature anomalies, reaching 1.30 °C and 1.29 °C for T_{min} and T_{max} respectively, on average over the Sahara; and 1.26 °C and 0.96 °C on average over the Sahel (to be compared to a mean springtime 90% quantile value which is respectively 3.06 °C, 3.59 °C, 2.66 °C and 2.69 °C above the climatology). Over the Sahel, they occur close to their climatological annual maximum, which leads to particularly high raw temperatures.

CERES incoming radiation fluxes SW_{in} and LW_{in} are averaged over each domain (Fig. 2c–f). Daily incoming longwave fluxes are significantly higher than shortwave fluxes (about 120 W/m^2 on average over the period). The variability of

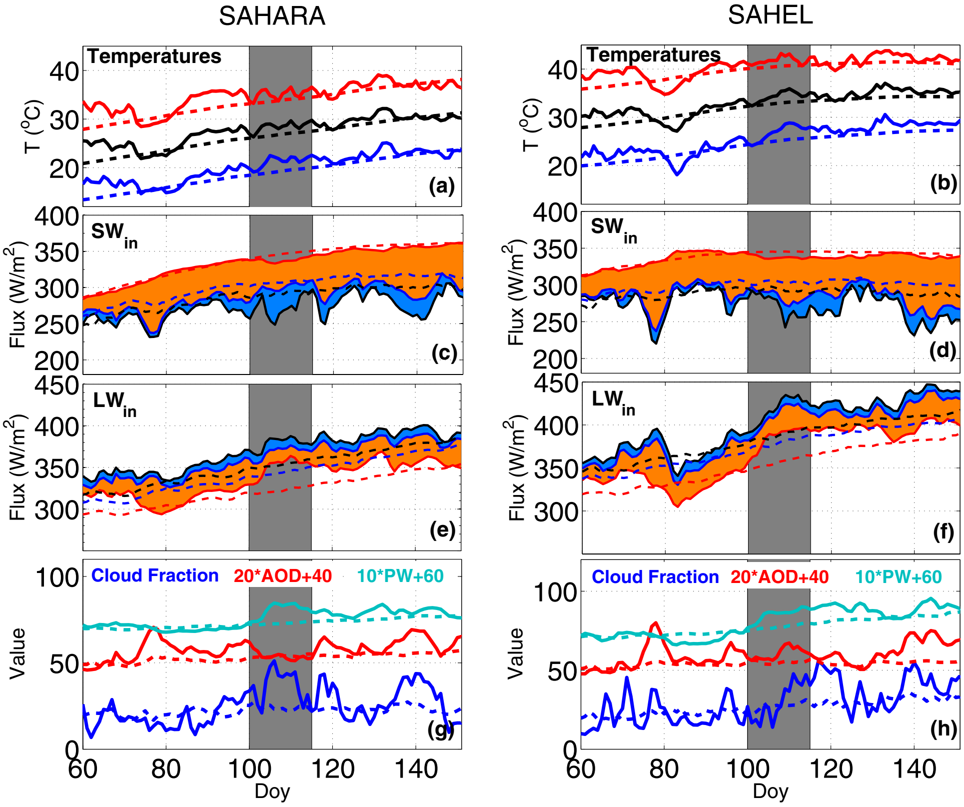

Fig. 2 Springtime time series of **a**, **b** T_{min} (blue), T_{avg} (black) and T_{max} (red); **c**, **d** daily-average SW_{in} (black), clear-sky SW_{in}^{clear} (blue), clean-sky SW_{in}^{clean} (red); blue shading therefore corresponds to the Cloud Radiative Effect and orange shading to the Aerosol Radiative Effect (see Sect. 4.1 for more details); **e**, **f** same as **c**, **d** for incoming longwave fluxes; and **g**, **h** Cloud fraction (in %, blue), 20*AOD+40 (red), 10*PW+60 (in cm, light blue). All values correspond to the average over the Sahara (left) or the Sahel (right). Solid lines: 2010 time series. Dashed lines: climatological time series. Grey shading: April 2010 Heatwave period

SW_{in} is driven by cloud cover and AOD fluctuations, which leads to strong synoptic and day-to-day modulations in the Sahel (Fig. 2d) whereas LW_{in} corresponding variability is weaker (Fig. 2f).

SW_{in} anomalies are persistently negative, near -15 W/m^2 on average over springtime for both domains. In contrast, LW_{in} anomalies are mostly positive during the period, reaching about $+18.5$ W/m^2 on average over springtime for both domains.

These anomalies are consistent with the increased cloud cover, AOD and PW observed during the period (Fig. 2g, h). Variations of SW_{in} are strongly coupled with the variations of cloud cover. Likewise, $SW_{in}^{clear-sky}$ is strongly related to AOD. By contrast, the fluctuations of LW_{in} appear more strongly related to those of PW. These correlations are even more pronounced when restricted to the heatwave period (grey shading on Fig. 2) that is further discussed in the next subsection.

3.3 Focus on the heatwave period

Recently, Barbier et al. (2018) developed a methodology to detect and track heatwaves over West Africa as intraseasonal events. They detect heatwaves when temperature intraseasonal anomalies exceed the 90% percentile of their local climatological distribution over a sufficiently extended area (greater than 6×10^5 km^2) for at least 3 consecutive days. For 2010, several heatwaves were identified when applying this methodology over the domain considered in the present study ([20° W, 20° E], [0° N, 30° N]) (e.g. Day Of Year (DOY) 60–75, 100–115, 125–135, see also Figure 2 in Barbier et al. (2018)). In the following, we focus on the heatwave event which occurred between 10 and 25 April, i.e. DOY 100 and 115. A significant part of the domain (about 24×10^5 km^2, i.e. 20% of the domain) was affected by this long-lasting event and furthermore, it occurred when temperatures were very high over the Sahel (Fig. 2b). Hereafter, this period is referred to as the heatwave period (HW, grey shading in figures). Note that the details of physical processes and mechanisms at play during springtime North African heatwaves are likely to vary from one event to another; in particular when considering late winter events (occurring in a very dry environment) or early monsoon events in late June (when the atmospheric water amount is on average higher). The period on which we focused here is more representative of North African heat waves occurring during the spring period when temperatures reach their annual maxima in the Sahel.

Increased T_{min} and T_{max} (and therefore T_{avg}) anomalies occur during this heatwave period, up to 4 °C over both the Sahel and Sahara. They coincide with reduced SW_{in} (anomalies up to -49 W/m^2) and strongly enhanced LW_{in} (anomalies up to $+44$ W/m^2). Note that the heatwave more strongly affects T_{min}, and is slightly stronger over the Sahara.

Table 3 Correlation coefficient r between two fields given in the left column over the Sahel (columns 2 and 4) and the Sahara (columns 3 and 5) during the heatwave period (10–25 April, column 2 and 3) and during the pre-heatwave springtime period (1 March to 10 April, columns 4 and 5)

Couples of variables	Heatwave		Pre-heatwave	
	Sahel	Sahara	Sahel	Sahara
T_{min} and LW_{in}	**0.97 (0.94)**	**0.85 (0.74)**	0.74	0.87
T_{min} and SW_{in}	-0.84 (-0.86)	0.01 (-0.46)	-0.20	0.55
T_{min} and AOD	0.82 (0.87)	-0.73 (-0.57)	0.22	-0.09
T_{min} and Cloud cover	0.77 (0.64)	0.37 (0.62)	0.16	0.59
T_{min} and PW	**0.84 (0.74)**	**0.85 (0.76)**	0.60	0.11
T_{max} and LW_{in}	0.62 (0.47)	0.22 (-0.09)	0.24	0.73
T_{max} and SW_{in}	-0.43 (-0.23)	0.53 (0.30)	0.43	0.76
T_{max} and AOD	0.59 (-0.39)	-0.69 (-0.45)	-0.40	-0.24
T_{max} and Cloud cover	0.25 (-0.03)	-0.30 (-0.24)	0.01	0.43
T_{max} and PW	0.36 (0.15)	0.25 (-0.04)	0.29	-0.09
LW_{in} and AOD	0.82 (0.85)	-0.62 (-0.31)	0.69	0.28
LW_{in} and Cloud cover	0.75 (0.49)	0.70 (0.93)	0.55	0.67
LW_{in} and PW	**0.87 (0.82)**	**0.95 (0.86)**	0.72	0.11
SW_{in} and AOD	-0.91 (-0.92)	-0.31 (-0.24)	-0.80	-0.33
SW_{in} and Cloud cover	**-0.82 (-0.72)**	**-0.82 (-0.87)**	-0.57	0.07
SW_{in} and PW	-0.66 (-0.61)	-0.16 (-0.44)	-0.49	-0.37

Values in parentheses are the correlation coefficient in terms of anomalies instead of raw values. Strongest correlations ($|r| > 0.8$ on both domains) are underlined with bold characters

Temporal correlation coefficients between all the fields shown in Fig. 2, both during the heatwave and pre-heatwave periods, are indicated in Table 3. Whereas all these fields display marked anomalies during the heatwave, day-to-day fluctuations are strongly positively correlated ($r > 0.8$ on both the Sahel and Sahara) only between T_{min} and LW_{in}, T_{min} and PW, LW_{in} and PW; (see bold values in Table 3). This suggests a tight link between nighttime temperatures, incoming longwave fluxes and precipitable water, both over the Sahel and Sahara, while every other covariations are less relevant. Note that during the pre-heatwave 40-day springtime period, these three correlations are significantly lower than during the heatwave period. This is particularly true over the Sahara where the strong link between PW and LW_{in} or T_{min} appears to be limited to the heatwave period. This highlights the impact of humidity during the heatwave, that will be further explored with the CNRM-AM and SARAWI models in Sects. 5 and 6. Table 3 also highlights that cloud cover has a direct influence on the reduction of SW_{in}, which is expected.

Positive correlations are also found between cloud cover and LW_{in} (or T_{min}), on average over both the Sahel and Sahara. Similarly, a significant positive correlation is found between AOD and LW_{in} (or T_{min}), but only over the Sahel (the correlation being negative over Sahara). However, these correlations should be interpreted with care. Indeed, cloud and aerosol longwave effects, that will be further explored in Sect. 4, will be shown to be unable to explain LW_{in} anomalies. Rather, these correlations are explained by covariations between PW and cloud cover (correlation of about 0.65), and between AOD and cloud cover over the Sahel (correlation of 0.74, due to the occurrence of dust events in Eastern Sahel and cloud intrusions in Western Sahel at the same time, not shown).

T_{max} fluctuations are not easily related to either incoming radiation fluxes, clouds, PW or aerosols. They are positively correlated with SW_{in} over the Sahara, while—surprisingly—negatively correlated over the Sahel during the heatwave. T_{max} fluctuations are also negatively correlated with cloud cover and AOD over Sahara, but positively over the Sahel. This suggests that T_{max} variations are probably explained by a complex interplay between various processes operating at different scales.

In summary, the April 2010 heatwave emerges from the climatology mainly because of the very high T_{min} prevailing during this 15-day period, while high T_{max} are restricted to a shorter duration (10 days) with weaker departure from the 90% percentile threshold. In the following, we focus mainly on the understanding of T_{min} anomalies.

3.4 Significant LW_{in} positive anomalies in T_{min} heatwave areas

The previously described strong positive correlation between daily-mean values of LW_{in} and T_{min} (or their anomalies, cf. Table 3) remains true at different time scales: spatially-averaged over the Sahel and Sahara, the correlation coefficient reaches $r = 0.99$ over the annual cycle, 0.96 over springtime and 0.90 over April 2010. This correlation can be further analyzed in space with Fig. 3, which shows LW_{in} anomalies for each day of the heatwave, overlaid by areas affected by the T_{min}-heatwave (in black

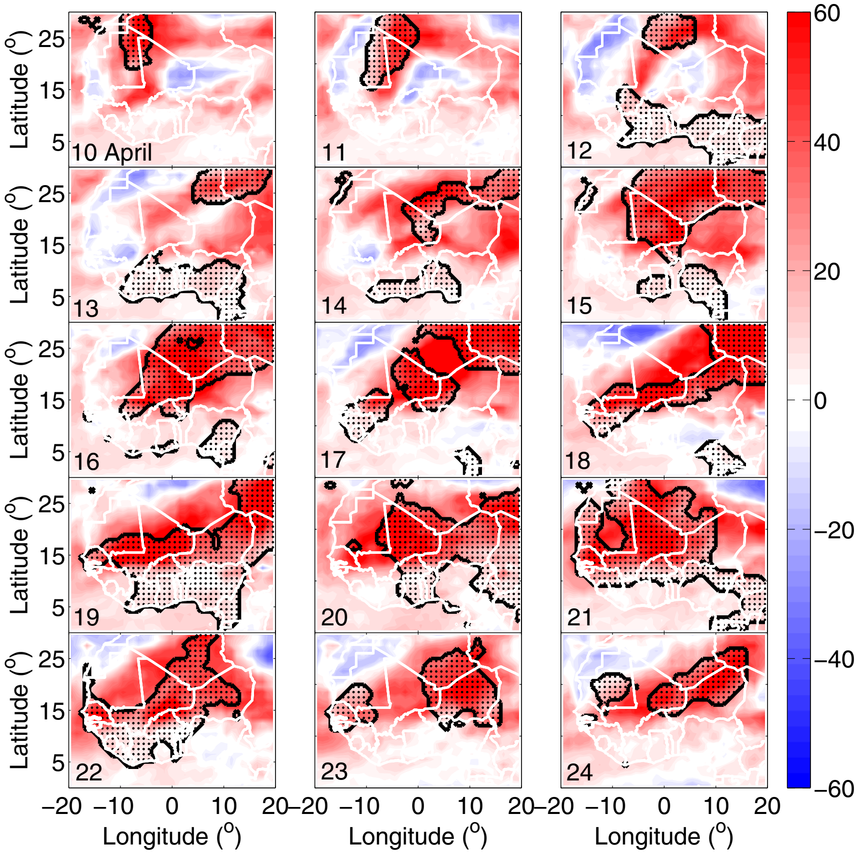

Fig. 3 Maps of the anomalies of the CERES daily incoming longwave flux, LW_{in} (color shading) superimposed with the areas affected by the heatwave, i.e. where T_{min} exceeds its local daily 90% percentile threshold (black dots), from 10 to 24 April 2010

contours). Strong T_{min} positive anomalies tend to overlay strong LW_{in} positive anomalies (up to 44 W/m^2), both over the Sahel and Sahara.

This relationship is however weaker over the Sudano-Guinean area, south to 12° N, which is the approximate location of the InterTropical Discontinuity (ITD) during springtime. There, T_{min} can reach anomalously-high values, with moderate LW_{in} anomalies (despite high LW_{in} raw values). This suggests that surface incoming longwave fluxes in the moister and wetter April Sudano-Guinean climate are less sensitive to fluctuations of water vapor and cloud cover than the driest April climate of Sahel and Sahara, in agreement with e.g., Stephens et al. (2012).

This also points out to distinct processes and mechanisms leading to heatwaves in the Sudano-Guinea region, while the link with LW_{in} clearly dominates in the Sahel and Sahara. Hereafter, we focus on the Sahel and Sahara.

4 Cloud and aerosol radiative effects

Here, we explore the radiative impacts of clouds and aerosols and show that, although strong positive anomalies of AOD and cloud cover are found respectively over the Sahel and Sahara, their radiative impacts are too weak to explain the anomalies of longwave fluxes.

4.1 Quantification of the cloud radiative effect (CRE) and aerosol radiative effect (ARE)

For any radiative flux F, the CERES database provides an estimate of the corresponding clear-sky (ie cloud free) $F_{clear-sky}$ and clean-sky (ie cloud and aerosol free) $F_{clean-sky}$ computed fluxes.

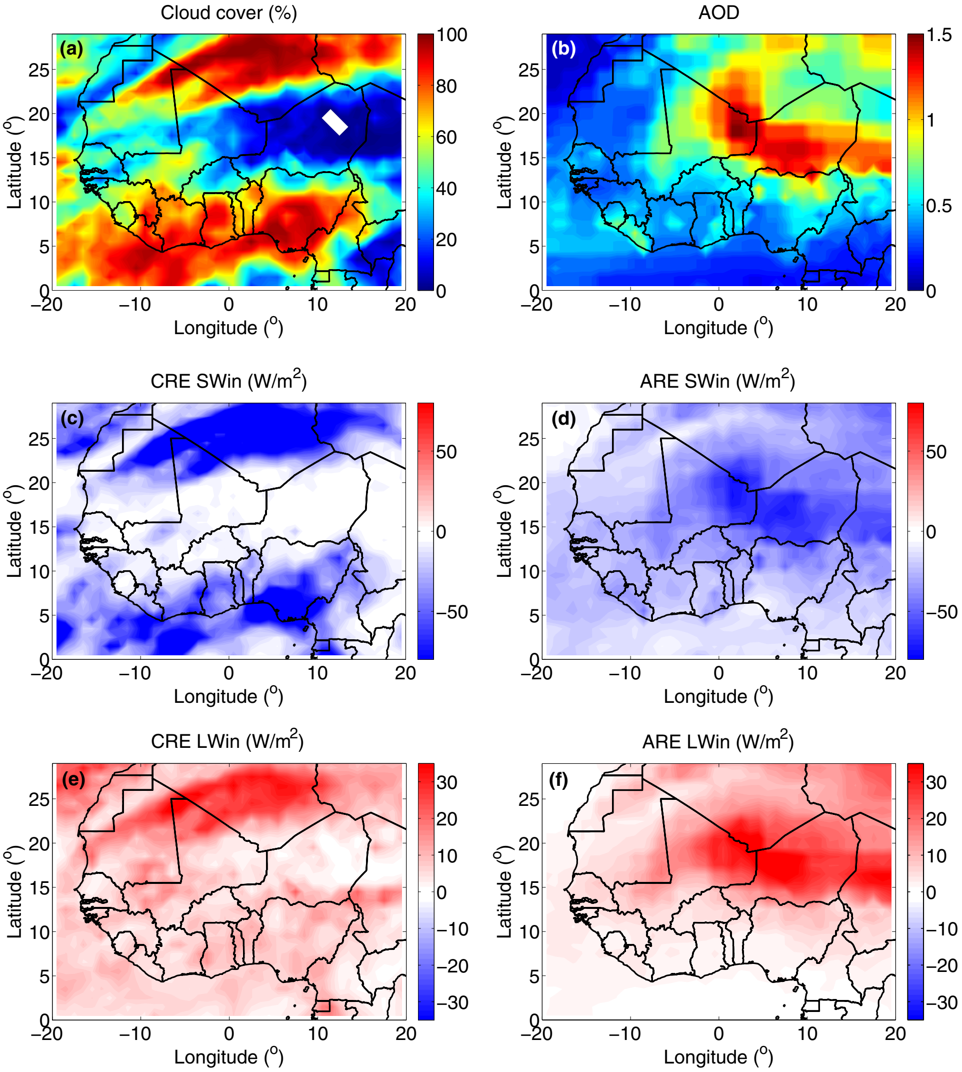

Fig. 4 Cloud c over area (%) (**a**) and AOD (**b**), CRE (**c**) and ARE (**d**) for SW_{in} (in W/m^2), CRE (**e**) and ARE (**f**) for LW_{in} (in W/m^2), over North Africa given by CERES on 15 April 2010, i.e. DOY 105

Following the definition of Ramanathan et al. (1989), the Cloud Radiative Effect (CRE) can be expressed as:

$$CRE = F - F_{clear-sky} \tag{10}$$

and similarly for the Aerosol Radiative Effect (ARE):

$$ARE = F_{clear-sky} - F_{clean-sky} \tag{11}$$

The Total Radiative Effect (TRE) is then:

$$TRE = CRE + ARE \tag{12}$$

4.2 Daily radiative effects during the heatwave

Figure 4 illustrates the daily-mean CRE and ARE in both the shortwave and longwave bands for 15 April 2010, i.e. DOY 105.

That day, the total cloud fraction is high over the northern Sahara, and the AOD is particularly strong over Niger, Eastern Mali and Southern Algeria (Fig. 4a, b).

Cloud cover and dust loadings both reduce incoming shortwave radiative fluxes at the surface, leading to negative shortwave CRE and ARE (Fig. 4c, d). In contrast, the incoming longwave radiative flux at the surface is increased below clouds and high dust loadings, leading to positive CRE and ARE, up to several tens of W/m^2 in these areas (Fig. 4e, f). This emphasizes how both aerosols and clouds can have a strong radiative impact over West Africa in spring.

4.3 Day-to-day evolution of ARE and CRE during the heatwave

On average over both the Sahel and Sahara, raw values of ARE are stronger than CRE both in the shortwave and longwave bands (Fig. 5). SW_{in} is reduced by about 20 W/m^2 with clouds and by another 50 W/m^2 with dust loadings. Conversely, LW_{in} is increased by about 10 W/m^2 with clouds and by another 25 W/m^2 with dust loadings.

During the whole spring 2010, large negative anomalies of shortwave ARE and positive anomalies of longwave ARE are observed, both over the Sahel and Sahara (Fig. 5). This is consistent with the positive anomaly of AOD (red curves in Fig. 2g, h) that increases both shortwave cooling and longwave warming. A few strong dust events occur during this period, for instance between DOY 75 and 80, when ARE reduces SW_{in} by 90 W/m^2 and increases LW_{in} by 55 W/m^2 over the Sahel. The heatwave period (grey shading in Fig. 5) is however less affected by the ARE over the Sahara (with anomalously low values in the longwave) and only slightly affected by a positive ARE anomaly over the Sahel, at the end of the period, between DOY 110 and 115.

Clouds have a lower radiative impact, both on longwave and shortwave fluxes, and the only significant CRE negative

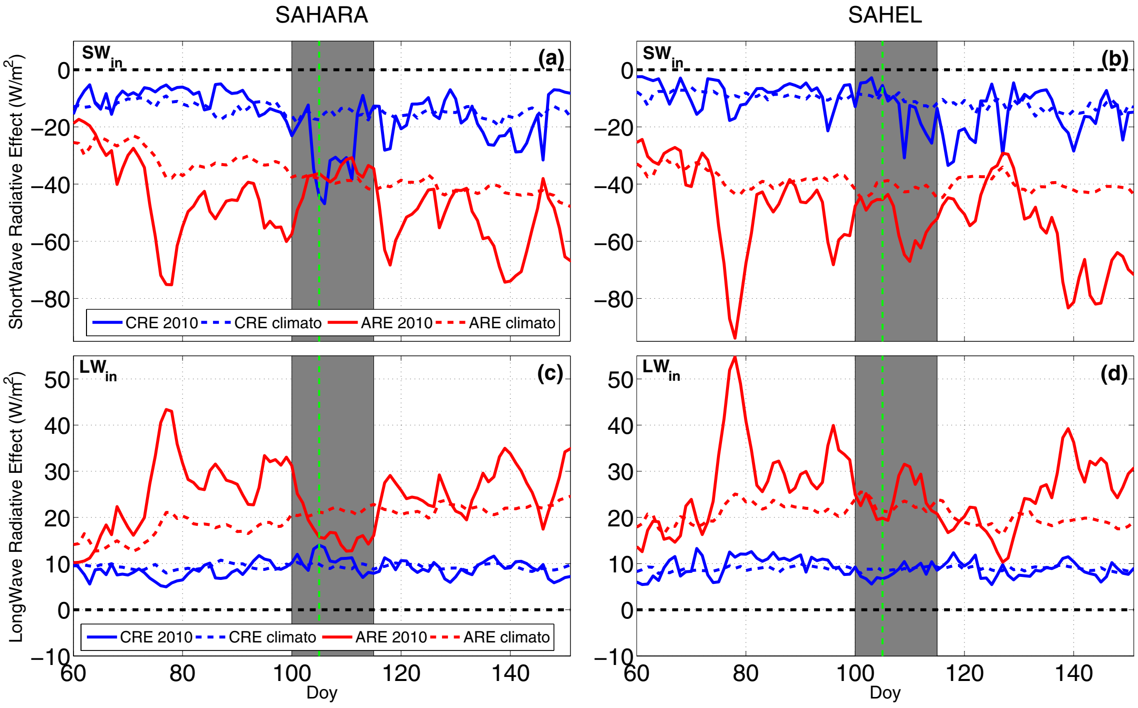

Fig. 5 springtime time series of incoming shortwave (**a**, **b**) and longwave (**c**, **d**) ARE (red) and CRE (blue), spatially averaged over the Sahara (left) and the Sahel (right). Solid lines: 2010. Dashed lines: climatology. The vertical dashed green line indicates 15 April 2010, shown in Fig. 4

anomaly is observed in the shortwave over Sahara during the heatwave (where it is driven by the tropical plume event) and over the Sahel at the end of the heatwave period. The longwave CRE remains close to its climatological values, without any notable anomaly during the heatwave.

4.4 Cloud and aerosol contributions to radiative anomalies

The ARE and CRE anomalies, together with the resulting TRE anomalies are compared to the incoming radiative flux anomalies in Fig. 6. For each region, the fraction of the incoming flux anomalies explained by either clouds or aerosols or the combination of the two is analyzed. Note that, since clouds reduce SW_{in} (cf. Fig. 5), a negative (respectively positive) anomaly of shortwave CRE does not correspond to a lower *radiative impact*, but means that clouds produce a *stronger reduction* (respectively a lower reduction) of the incoming fluxes in 2010 than usual at the same day. Similarly, since clouds increase LW_{in}, a positive (resp. negative) anomaly of longwave CRE means that clouds produce a stronger increase (resp. a lower increase) of the incoming fluxes in 2010 than usual at the same day. Same conclusions can be dressed for ARE.

During the heatwave, a strong negative anomaly of SW_{in} is observed (Fig. 6a, b). It is almost entirely explained by clouds over the Sahara, and by a combined effect of clouds and aerosols in the Sahel (with a larger contribution from aerosols though). Note that the 15-day period following the heatwave is also marked by a strong negative anomaly of SW_{in}, which, in contrast, is almost entirely explained by aerosols in the Sahara.

The heatwave is characterized by a wide and strong positive anomaly of LW_{in} (about 25 W/m^2 in the Sahara and 30 W/m^2 in the Sahel, cf. Fig. 6c, d). CERES surface radiative fluxes estimates do not support that clouds and aerosols might drive this positive anomaly, as they even contribute to a negative anomaly over the Sahara and to a very weak ARE positive anomaly of 1.5 W/m^2 over the Sahel, which roughly corresponds to only 5% of the total LW_{in} anomaly. Conversely, this anomaly of LW_{in} is strongly correlated to that of PW (Table 3 and Fig. 6e, f), which suggests that the radiative effect of water vapor contributes to the emergence of this LW_{in} anomaly. This water vapor radiative effect will be further investigated in details with the SARAWI model in Sect. 6.

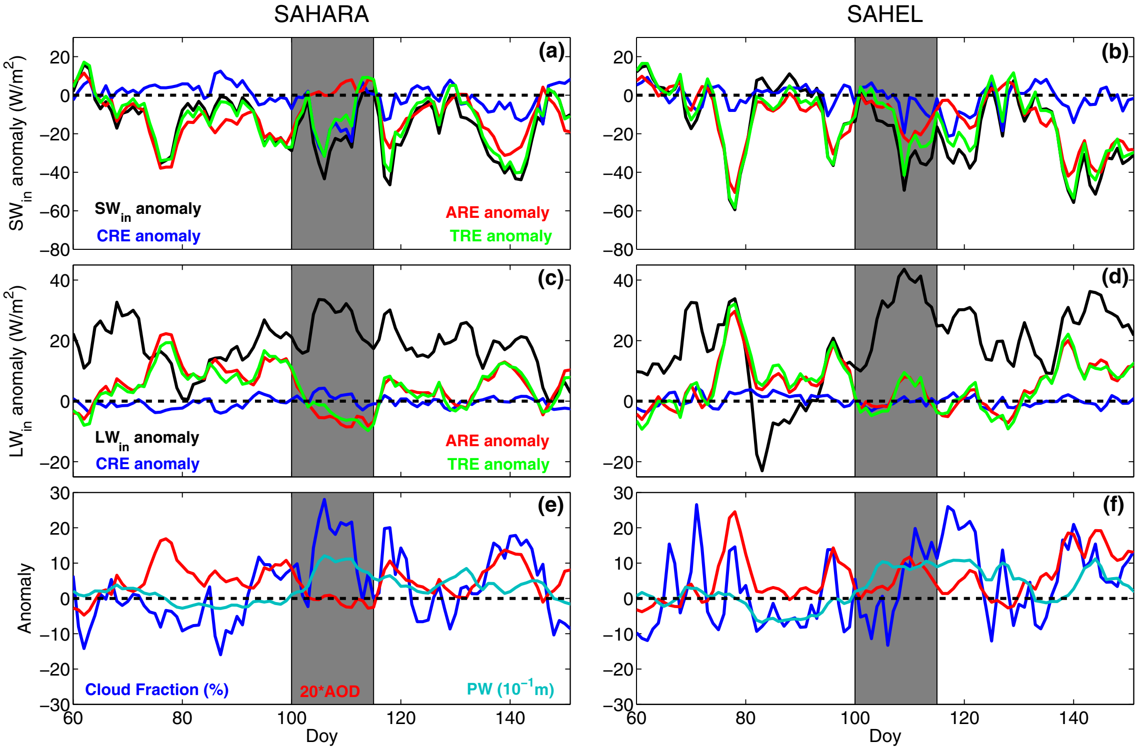

Fig. 6 springtime time series of anomalies of: shortwave fluxes and shortwave ARE, CRE, TRE (**a**, **b**), longwave fluxes and longwave ARE, CRE, TRE (**c**, **d**), cloud fraction, AOD and PW (**e**, **f**), averaged over the Sahara (left) and the Sahel (right)

5 Nudged climate model simulation results

In this section, boundary-layer physics is explored using climate simulations performed with CNRM-AM. We show that the 2-m temperature is driven by turbulence and longwave radiation, and that the latter drives its nighttime evolution. Atmospheric longwave emissivity is found to be closely related to 2-m specific humidity.

5.1 Maps of fluxes and temperature during the heatwave

The dynamical nudging towards ERA-interim fields prevents strong departures of the CNRM-AM simulation from observations and allows to follow the realistic chronology of the heatwaves events. Indeed, the annual cycles of T_{min} and T_{max} and their spatial variability over North Africa are well correlated to observed values (the mean correlation coefficient over the 222 SYNOP ground-stations included in the considered domain is around 0.75 for T_{min} and T_{max}). The annual averaged bias over these stations also remains small, −0.06 °C for T_{min} and −0.4 °C for T_{max}. Note that at smaller-scale, biases nevertheless become larger. For instance, in the Sahelian belt during the heatwave, T_{min} is underestimated (by up to 2.5 °C) at some ground-stations.

In line with the results of Sane et al. (2012), Hourdin et al. (2015) and Diallo et al. (2017) which also constrained the atmospheric dynamics of their GCM simulations by a high-frequency nudging of the wind towards meteorological reanalyses, our CNRM-AM nudged simulation is also able to capture the main observed spatial patterns at a daily time scale. A typical comparison between the observed and simulated daily-mean SW_{in} and LW_{in} fluxes, T_{max} and T_{min}

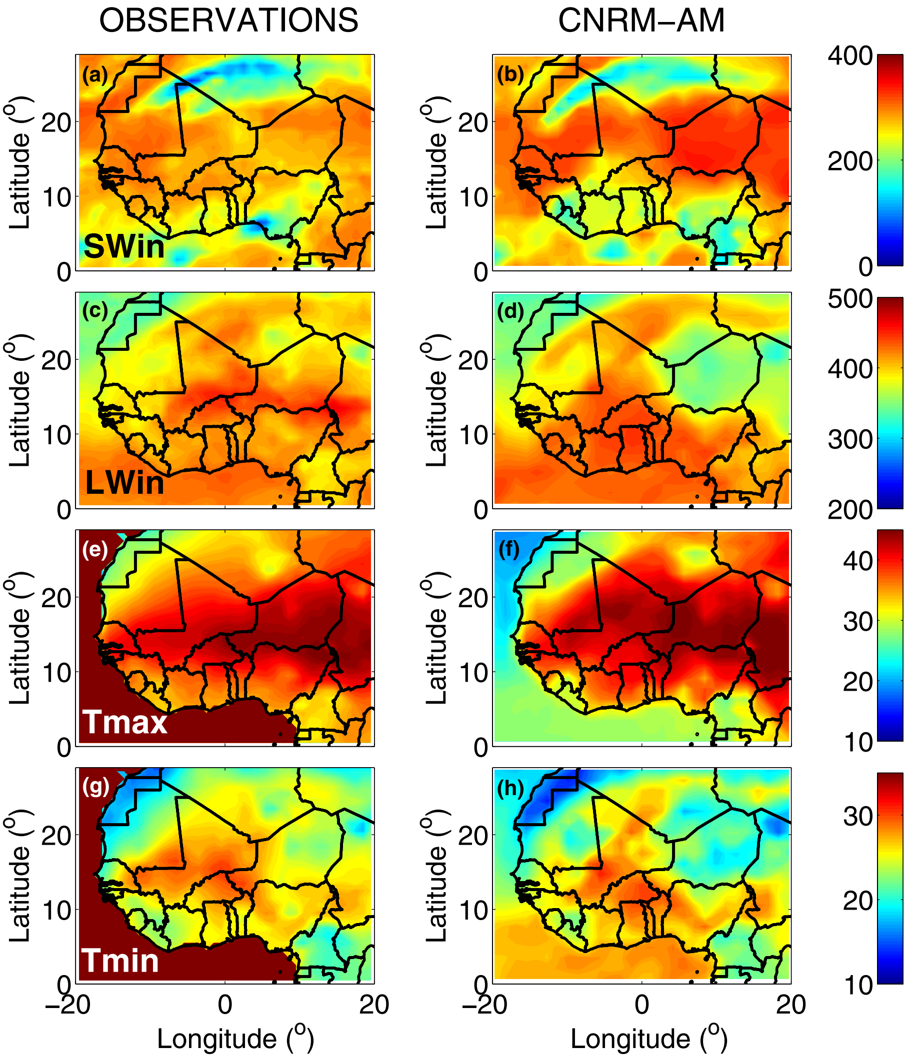

Fig. 7 Incoming shortwave flux SW_{in} (**a**, **b**) and longwave flux LW_{in} (**c**, **d**) at the surface in W/m^2; T_{max} (**e**, **f**) and T_{min} (**g**, **h**) in °C over North Africa given by CERES or BEST observations (left) and CNRM-AM simulation (right) on 15 April 2010, ie DOY 105. Note that there is no data in ocean on **e** and **g**

temperatures is shown in Fig. 7, for 15 April 2010 (same day as Fig. 4).

The main features of the incoming fluxes and radiative effects of clouds (dominantly present in Northern Sahara, Fig. 7) are well-captured by CNRM-AM (Fig. 7a–d), especially in terms of spatial patterns. Similarly, T_{max} patterns are well reproduced, with the hottest areas located in the Sahel and southern Sahara and the colder area near the western Saharan coast (Fig. 7e, f). The strong T_{min} values are also reasonably simulated, both over Mali and northern Sahara, consistently with the realistic simulation of the strong nighttime LW_{in} (partly due to the high-level clouds present that day, Fig. 4a).

However, some biases can be noticed, mainly located in Niger and Chad, where SW_{in} is overestimated and LW_{in} underestimated. These biases could be related to AOD differences. Indeed, CNRM-AM uses a climatological monthly-mean AOD, whereas AOD on that day (15 April 2010) exhibits a strong anomaly over these areas (Fig. 4b). As a consequence, the strong observed longwave and shortwave ARE are most likely missed by the model on this day, which leads to overestimated T_{max} and underestimated T_{min} over Niger and Chad (Fig. 7f, h).

5.2 Fluctuations of temperature, humidity and fluxes in the Sahel during the heatwave: comparison with in-situ data

A comparison between simulated and observed time series of temperature, specific humidity and radiative fluxes is presented in Fig. 8, at Agoufou, Mali (see location in Fig. 1b), within the Sahelian area significantly affected by the heatwave (Fig. 3). Here, we used the simulated fields at the closest grid point to the observational site (15°20′40″ N and 1°28′45″ W).

Before DOY 103, Agoufou is located north of the ITD, the low-atmospheric layers are dry ($q_v < 3$ g/kg) and the surface air temperature is high during daytime (> 40 °C) but sharply drops at night, down to 23 °C (Fig. 8a). SW_{in} is strong during daytime while LW_{in} (and LW_{net}) decreases to relatively low values during nighttime (Fig. 8b, d, e). The

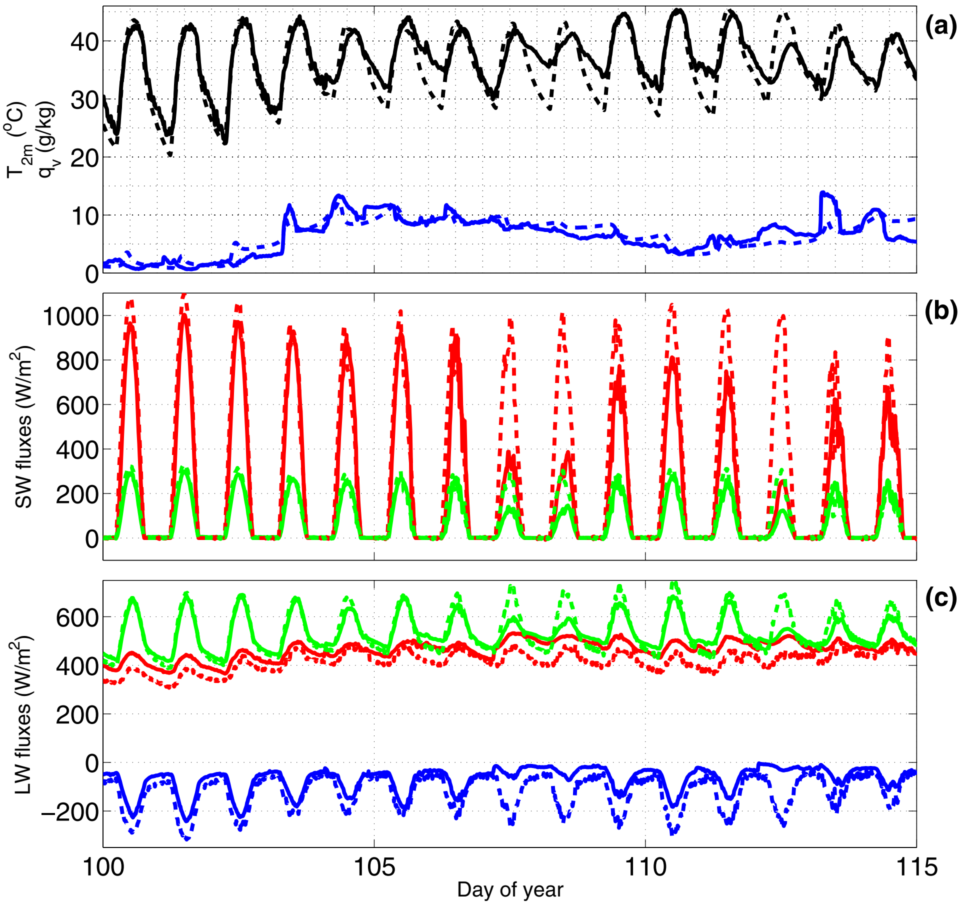

Fig. 8 Time series of: **a** 2-m air temperature (black) and specific humidity (blue); **b** SW_{in} (red) and SW_{up} (green); **c** LW_{in} (red), LW_{up} (green) and LW_{net} (blue) at Agoufou during the heatwave. Solid lines: local ground observations. Dotted lines: CNRM-AM simulation

Diurnal Temperature Range (DTR) is large, around 20 °C before DOY 103.

In-situ observations at Agoufou in 2010 illustrate the impact of the arrival of the monsoon flow in the Sahelian belt (this flow migrates northward during springtime, Couvreux et al. 2010): its first incursion occurs on DOY 103. Once the flow has reached the site, atmospheric water vapor increases, and simultaneously, nighttime temperatures, LW_{in} and LW_{net} increases ($T_{min} > 30$ °C). The following 12 days match the local heatwave period, during which daytime SW_{in} is reduced and displays a much stronger day-to-day variability due to the cloud cover. It leads to much lower T_{max} and DTR during cloudy days. During clear-sky days, DTR is significantly reduced compared to the pre-heatwave period while T_{max} remains close to its pre-heatwave values (40–45°C). The daily-average temperature increase is dominantly driven by that of T_{min} during this heatwave, whereas T_{max} is only weakly affected by the change of environmental air masses.

The incursions of the monsoon flow, as seen by the increase of 2-m specific humidity are correctly reproduced by CNRM-AM (dotted lines in Fig. 8a). The dynamical nudging thus allows to well constrain the location of the ITD, at least around Agoufou. Consistently, the increase of T_{min} concomitant with this moistening is also realistically captured, with T_{min} increasing by about 10 °C between the pre-heatwave and the heatwave periods. The simulated diurnal fluctuations of radiative fluxes, specific humidity and temperatures are also close to observations, despite some biases, most likely due to the representation of clouds and can be summarized as follows:

1. Day-to-day variability of SW_{in} is underestimated during the heatwave period (especially during the cloudy period from DOY 107 to 112, Fig. 8b). Since shortwave CRE seems reasonably well reproduced with CNRM-AM (not shown), this overestimation of SW_{in} points towards either an underestimation of the cloud cover at this site, or an incorrect phasing in the diurnal cycle of cloud cover.
2. Consistently, the DTR is overestimated during the heatwave cloudy days.
3. Finally, LW_{in} is underestimated throughout the diurnal cycle, while LW_{up} is closer to observations, except for cloudy days for which the simulated SW_{in} leads to an overestimation of the land surface temperature and LW_{up}. Their combination induces an underestimated LW_{net}, more pronounced during cloudy days.

Even though it remains difficult to draw firm conclusions regarding the role of clouds during the heatwave, especially because of the shortcomings resulting from the comparison between local measurements and a model grid pixel of 1.4°, CNRM-AM is able to capture part of the major observed characteristics of the T_{min} and LW_{in} evolutions, especially their synchronous increase when the monsoon flow reaches Agoufou. CNRM-AM can thus be used to further understand part of the role of water vapor in the T_{min} evolution. Note however that the increase in T_{min} and LW_{in} are weaker in CNRM-AM, which suggests an underestimation of the impact of humidity on 2-m temperatures and longwave fluxes. The SARAWI model will be used in Sect. 6 to further explore this humidity impact.

5.3 Physical processes acting at local scale: the impacts of turbulence and longwave radiation

In order to investigate the processes at play in the low atmospheric layers, we analyze the daytime and nighttime temperature budgets in the first atmospheric layer of the CNRM-AM simulation. Figure 9 shows the daytime and nighttime variations of temperatures for each day of April 2010 (purple) by "at the nearest gridpoint to Agoufou, together with the contribution of each physical process to the thermodynamic equation: boundary-layer turbulence, longwave and shortwave radiation, large-scale precipitation and condensation, parameterized deep and shallow convection, and advection (here, they are cumulated either over the daytime hours, i.e. from sunrise to sunset, or nighttime hours). The total temperature variation (purple) is the sum of each of the previously listed contributions.

The CNRM-AM nocturnal cooling is almost entirely due to longwave radiation (Fig. 9b), whereas its daytime warming mainly results from the balance between the longwave radiative warming and the turbulent cooling (Fig. 9a). Surprisingly, during daytime, the longwave warming dominates the temperature variation at the first atmospheric level and overcompensates the turbulence. The net daytime effect of turbulence is to cool the first atmospheric level. This cooling mainly acts in the afternoon by vertical mixing of the first layer with the colder layers above (more details in Sect. 6.1 and Fig. 11). The temperature advection only plays a minor role in the evolution of the first air layer temperature. Therefore, the fluctuations of surface air temperature during the heatwave episode are dominantly driven by longwave radiative and turbulent processes.

Figure 10a, b illustrates the evolution of the nighttime surface energy budget. This nighttime budget is dominated by the net radiative cooling $R_{net} = LW_{net}$, and very slightly compensated with a weak warming from the surface by the sensible heat flux (Fig. 10a). Note that, after DOY 103, when the ITD overpasses Agoufou, the nighttime net cooling R_{net} weakens, compared to the pre-heatwave period. Both LW_{in} and LW_{up} increase, but LW_{in} increases more than LW_{up}, which leads to an increase in LW_{net} and enhances the radiative coupling between the surface and the lower troposphere.

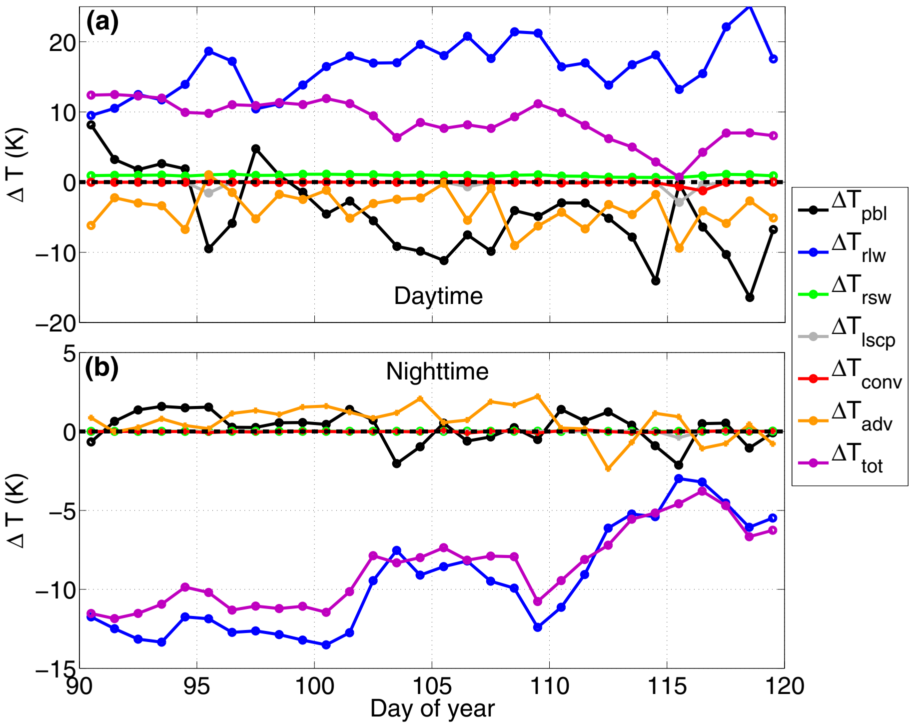

Fig. 9 Time series of daytime (**a**) and nighttime (**b**) ΔT temperature variation at the first atmospheric level (purple) and the corresponding contribution of each physical parameterization during April 2010 at Agoufou, in CNRM-AM simulation. Black: planetary boundary layer (pbl); blue: radiative longwave (rlw); green: radiative shortwave (rsw); grey: large-scale condensation and precipitation (lscp); red: deep and shallow convection (conv); orange: advection (adv)

This further induces a weaker nighttime cooling of the lower atmospheric layer (Fig. 9b).

5.4 Impact of water vapor on atmospheric longwave emissivity

The land surface longwave emissivities ϵ_s can be retrieved from:

$$LW_{up} = \sigma.\epsilon_s.T_s^4 \tag{13}$$

We can also estimate an atmospheric "effective" longwave emissivity ϵ_a from LW_{in} and the temperature of the lower layer (e.g. Prata 1996 among others), using:

$$LW_{in} = \sigma.\epsilon_a.T_a^4 \tag{14}$$

Figure 10c illustrates the April 2010 time series of the nighttime values of ϵ_s (red) and ϵ_a (black), computed from CNRM-AM fields. The evolution of this air longwave emissivity ϵ_a at Agoufou is strongly correlated ($r = 0.94$) with the nighttime average 2-m specific humidity (Fig. 10c, d). Note that this correlation still holds at smaller time-scales (not shown). It illustrates the increase of longwave emissivity associated with an increase of the amount of water vapor. The time series of ϵ_a is well-approximated by the linear regression using 2-m specific humidity and 2-m air temperature presented in Eq. 9 (with values of a_i fitted at Agoufou, blue curve in Fig. 10c).

6 Insights from a conceptual prognostic model: quantification of a humidity radiative effect (HRE)

Here, the SARAWI model presented in Sect. 2.5 is used to investigate further the impact of water vapor. To this end, we introduce a Humidity Radiative Effect (HRE, detailed in Sect. 6.3). SARAWI explicitly parameterizes the effect of water vapor on the air longwave emissivity (Eq. 9).

This model assumes that synoptic and regional scale motions associated with the monsoon flow and the tropical plume can be decoupled from physical processes operating at local scale, and therefore the CNRM-AM wind and specific humidity fields are used as inputs to the SARAWI model. Then, the model directly solves the effects of turbulence and radiative transfer between the soil and the atmospheric surface layer, as these two processes have been identified as the major drivers of the temperature fluctuations (Sect. 5).

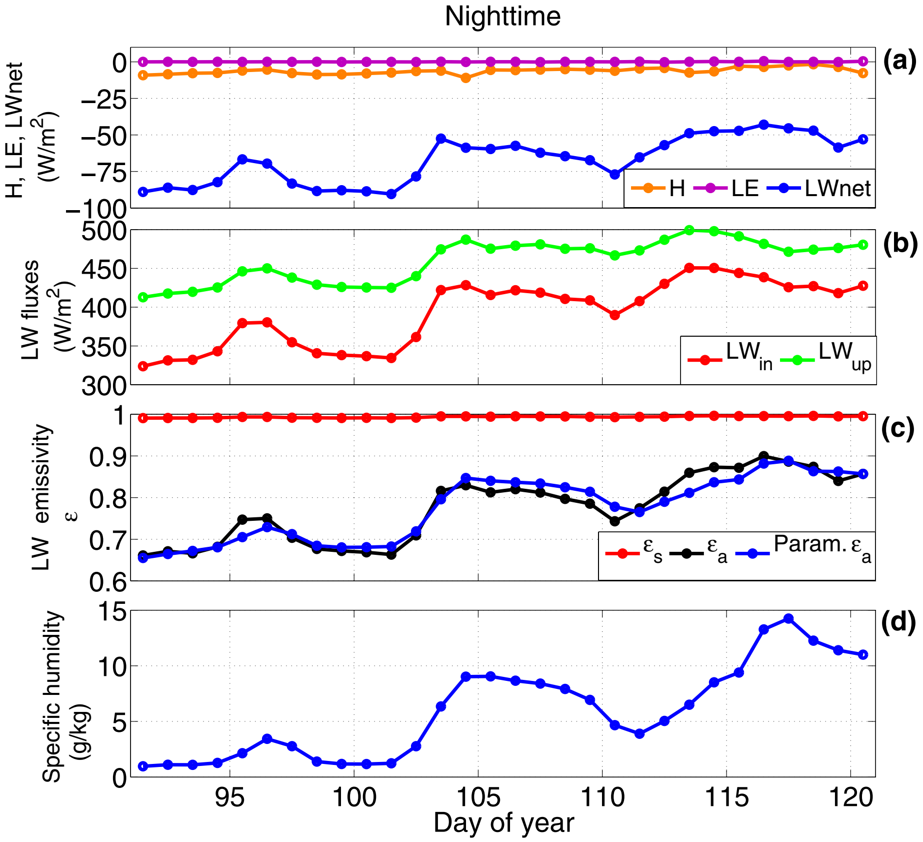

Fig. 10 Time series of nighttime surface fluxes H, LE and LW_{net} (**a**), LW_{in} and LW_{up} (**b**), ϵ_s, ϵ_a and parameterized ϵ_a, cf. Sect. 5.4 (**c**), and 2-m specific humidity (**d**) in April 2010 at Agoufou, in the CNRM-AM simulation

Simulations are performed with SARAWI over April 2010, either in 1D at the site of Agoufou or in 3D over North Africa.

In the following, we first evaluate the time evolution of the SARAWI variables given in Eqs. (1)–(8) with the help of the CNRM-AM simulations (Sect. 6.1) before evaluating the 3D SARAWI computation over North Africa (Sect. 6.2). Then, another simulation is made with a constant specific humidity field to evaluate an HRE at Agoufou during the heatwave (Sect. 6.3), and over North Africa (Sect. 6.4). Finally, we demonstrate that the observed anomaly of LW_{in} in North Africa can be explained by means of the HRE quantified with SARAWI (Sect. 6.5).

6.1 Evaluation of the representation of turbulence and longwave radiation

Figure 11 presents a comparison of the time evolution of ${\frac{\partial T_a}{\partial t}}_{rlw}$, ${\frac{\partial T_a}{\partial t}}_{pbl}$, LW_{net} and H simulated by CNRM-AM and SARAWI at Agoufou, zoomed over a 5-day window during the heatwave period. This period is centered around DOY 103, which corresponds to the first incursion of the monsoon flow at the site. It is chosen to point out the evolution of the diurnal cycles during the transition from the pre-heatwave towards the heatwave period, but a similar good match between SARAWI and CNRM-AM outputs is found throughout April 2010 (see Fig. 13 detailed in the following sections).

Indeed, SARAWI faithfully replicates the diurnal fluctuations simulated by CNRM-AM, for the four parameterized fluxes and temperature tendencies. Similarly, time series of T_s, T_{2m} and T_a given by SARAWI are very close to those computed by CNRM-AM (Fig. 11e,f), with only minor deviations (the mean biases over April 2010 are 0.15 °C, 0.5 °C and 0.9 °C respectively for T_a, T_{2m} and T_s, with $r > 0.98$ for all three temperatures).

SARAWI also reproduces quite well the transition between the pre-heatwave regime (higher DTR, stronger nighttime air radiative cooling, lower daily-mean LW_{net}) and the heatwave regime (lower DTR, lower nighttime air radiative cooling, higher LW_{net}). This ability of SARAWI to reproduce this transition points out the crucial impact of atmospheric water vapor on longwave air emissivity, and thus on the increase of temperature and fluxes. From these

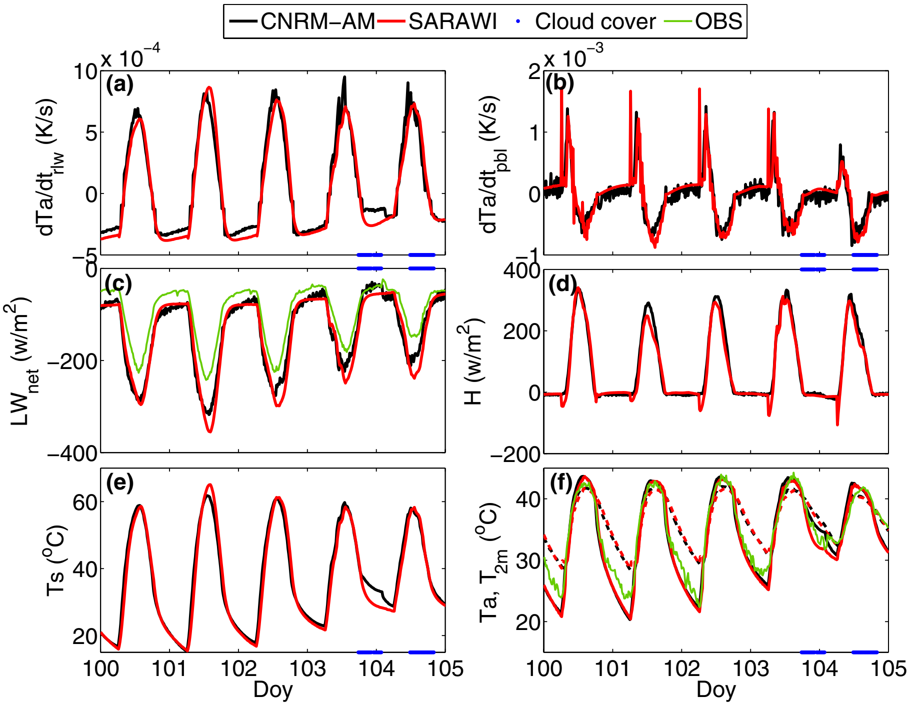

Fig. 11 Time series of $\frac{\partial T_a}{\partial t}_{rlw}$ (**a**), $\frac{\partial T_a}{\partial t}_{pbl}$ (**b**), LW_{net} (**c**), H (**d**), T_s (**e**) and T_a (f, dotted lines) and T_{2m} (**f**, solid lines) for 5 days of the heatwave at Agoufou, in SARAWI (red) and CNRM-AM simulation (black). Blue dots at the top or bottom of panels indicate the presence of clouds in CNRM-AM. Observed LW_{net} and T_{2m} are superimposed in green in **c** and **f** respectively

results, the following scenario, which implies a water vapor greenhouse effect, can be formulated:

1. The increase of specific humidity associated with the monsoon flow increases ϵ_a, that in turn increases LW_{in}.
2. This increase of LW_{in} increases the radiative warming of the soil surface layer, and thus also T_s (Fig. 11e)
3. Synchronously, the increase of T_s leads to an increase of LW_{up}.
4. LW_{in} however increases more than LW_{up}, which leads to an increase of LW_{net} (Fig. 11c).
5. The increase of LW_{in} corresponds to a loss of energy for the air layer, but this loss is more than compensated by an increased infrared absorption of LW_{up} in this layer. Indeed, the latter is enhanced by both higher LW_{up} and air absorptivity (equal to ϵ_a); whereas the former is solely increased by higher ϵ_a.
6. This finally results in less nighttime radiative cooling of the air layer and therefore in a higher T_a in the heatwave period than before.

This water vapor greenhouse effect involves a positive feedback: higher LW_{in} leads to a warmer surface, which in turns leads to a warmer air layer, and therefore higher LW_{in}. The magnitude of this feedback is limited as higher LW_{in} also means a loss of energy of the air layer, which negatively feeds back on T_a. The resulting heatwave equilibrium involves a balance between these two feedbacks, which happens on a very short timescale, during the first heatwave night.

SARAWI exhibits few departures from CNRM-AM, mainly during the night of DOY 104, due to the presence of clouds in the CNRM-AM simulation (cf. blue dots in Fig. 11). Cloud longwave radiative effects are not represented in the SARAWI model, and that night, the presence of clouds is associated with enhanced LW_{in} in CNRM-AM, which leads to higher T_s and T_{2m} than in SARAWI (the differences reaches up to 3 °C). Interestingly, these SARAWI biases provide inferences on the longwave CRE both on fluxes and temperatures.

Finally, the available observations at Agoufou are superimposed in blue in Fig. 11. The observed LW_{net} is underestimated by both CRNM-AM and SARAWI due to an underestimation of LW_{in}, throughout the diurnal cycle, as discussed in Sect. 5.2. Nevertheless, the observed T_{2m} is quite well reproduced with CNRM-AM and SARAWI, except towards the end of the night. This can be explained as follows: the daytime underestimation on LW_{net} has a low impact of T_{2m} since shortwave fluxes are significantly stronger so that the daytime energy budget is dominated by shortwave which is correctly reproduced with these models. However, the nighttime underestimation of LW_{net} leads to a stronger cooling and therefore to a slightly underestimated end-of-night T_{2m}. Note that the underestimation of LW_{in} is due to an underestimation of ϵ_a, which could be solved in SARAWI if Eq. (9) was regressed with observed data, rather than with CNRM-AM data as done in the current version of the model.

6.2 Maps of T_{min} and longwave fluxes over North Africa

SARAWI is further used in a 3D mode over North Africa. The main geographical patterns of T_{min} and LW_{net} given by CNRM-AM are well reproduced by SARAWI. An example is shown in Fig. 12 for 15 April 2010. Similar results are found for every days of April.

The most notable biases are found in the northern Sahara for T_{min} and LW_{net}, which are most likely related to the neglect of longwave CRE in SARAWI. There, the cloud cover is high in both observations and CNRM-AM, and induces significant longwave CRE and nighttime warming (Figs. 4 and 7).

Apart from those cloud-related impacts, the agreement between CNRM-AM and SARAWI over the region, both in terms of patterns and orders of magnitude, validates the hypotheses at the heart of the SARAWI model, and underlines the nature of the scale interactions between large-scale circulations and local physical processes: the dynamics of the monsoon flow and that of the tropical plume event over the Sahara, drive regional and synoptic-scale advection of atmospheric water vapor. From there, radiative and turbulent processes, which act at local and subdiurnal scales, subsequently drive the evolution of the longwave fluxes, soil and low-level air temperatures.

In summary, the high nighttime temperatures observed during the heatwave do not result from some synoptic advection of warm air masses (since synoptic advection is neglected in Eq. (1)). Rather, the synoptic advection of water vapor is the most important component as it increases the low-level air opacity and emissivity (that explicitly depends upon the specific humidity and is prescribed in SARAWI, through Eq. (9)). This results in an increase of T_{min}, which is dominantly controlled by atmospheric radiative transfer and boundary-layer turbulence, since they are the only processes parameterized in SARAWI (Eq. (1)).

6.3 Quantification of the humidity radiative effect (HRE)

Figure 13 shows, for April 2010 at Agoufou, time series of LW_{in} (a), T_{2m} (b), T_{max} (c, dashed lines) and T_{min} (c, solid lines) computed by SARAWI (red), and CNRM-AM (black). The high correlation between the CNRM-AM and SARAWI time series echoes the results presented in the previous section. Differences between CNRM-AM and SARAWI only occur during the most heavily cloudy days (blue dots in Fig. 13).

An additional 3D simulation is performed with SARAWI where specific humidity remains constant in time; for each grid point, it equals its nighttime average value on 1 April 2010 (hereafter referred to as hus_0). On 1 April 2010, the specific humidity field displays high values

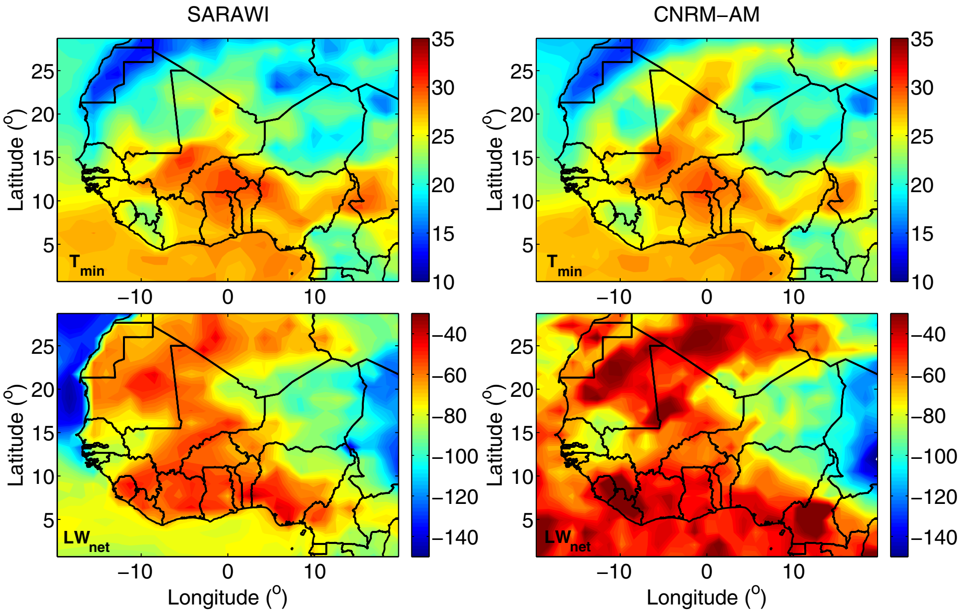

Fig. 12 T_{min} (**a**, **b**) and LW_{net} (**c**, **d**) fields given by SARAWI (left) and CNRM-AM (right) on 15 April 2010, ie DOY 105

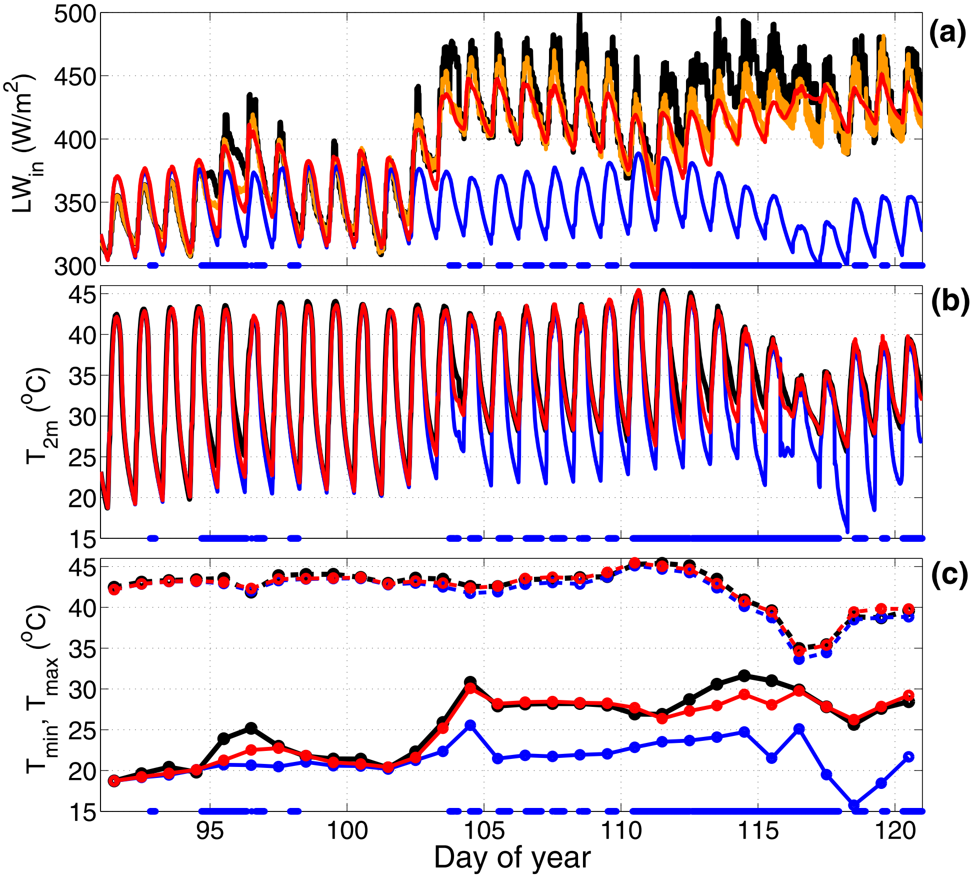

Fig. 13 Time series at Agoufou for April 2010 of: LW_{in} (**a**), T_{2m} (**b**), T_{max} (**c**, dashed lines) and T_{min} (**c**, full lines). Black: CNRM-AM. Red: SARAWI reference simulation. Blue: SARAWI simulation with constant humidity. Orange: clear-sky LW_{in} computed by CNRM-AM. Blue dots at the bottom of panels: cloud cover in CNRM-AM

south of the ITD (around 12° N), within the monsoon flow, and much lower values north of the ITD. At Agoufou, located north of the ITD on 1 April, the specific humidity remains low, around 1 g/kg, which is close to its dry season average. The humidity radiative effect associated with the increase of ϵ_a during the heatwave is therefore discarded in this simulation, whose results are shown in blue in Fig. 13.

LW_{in} and T_{2m} are very close to their values in the reference simulation until DOY 103. Afterwards, during the heatwave, the two simulations diverge. In the constant moisture simulation, little change in the diurnal fluctuations before and after DOY 103 is simulated, at least until DOY 115 (Fig. 13). Overall, daily maxima are close to their values in the reference SARAWI simulation, but the nighttime characteristics of the heatwave period are not reproduced in the constant moisture simulation; LW_{in} and T_{min} remain significantly lower, which reveals the strong sensitivity of the system to the specific humidity.

The temperature variation due to the Humidity Radiative Effect is further quantified with: $\Delta T_{min}^{HRE} = T_{min} - T_{min}^{hus_0}$ where $T_{min}^{hus_0}$ is the value of T_{min} in the constant humidity simulation. Similarly, we define $\Delta LW_{in}^{HRE} = LW_{in} - LW_{in}^{hus_0}$ for quantifying the HRE on the incoming longwave flux. At Agoufou, the averaged ΔLW_{in}^{HRE} during the heatwave reaches $59 W/m^2$, associated with an averaged ΔT_{min}^{HRE} of 4.75 °C, that reaches values higher than 6.5 °C between DOY 105 and 109.

When compared to the observed estimates of longwave CRE and ARE (Fig. 5) which are respectively of 15 and 19 W/m^2 on average during the heatwave at Agoufou, the current estimate emphasizes that HRE stands as the dominant driver of the nighttime warming. According to those estimations, HRE explains 64% of the total radiative warming during the heatwave, while ARE explains 20% and CRE 16%, and HRE leads to a nighttime increase of 2-m temperature up to 6.5 °C, at Agoufou.

6.4 Maps of the HRE over North Africa

The spatial structure of ΔLW_{in}^{HRE} and ΔT_{HRE} is shown in Fig. 14a, b for the 15 April 2010 at 06 UTC, together with the specific humidity field (Fig. 14d) and the difference

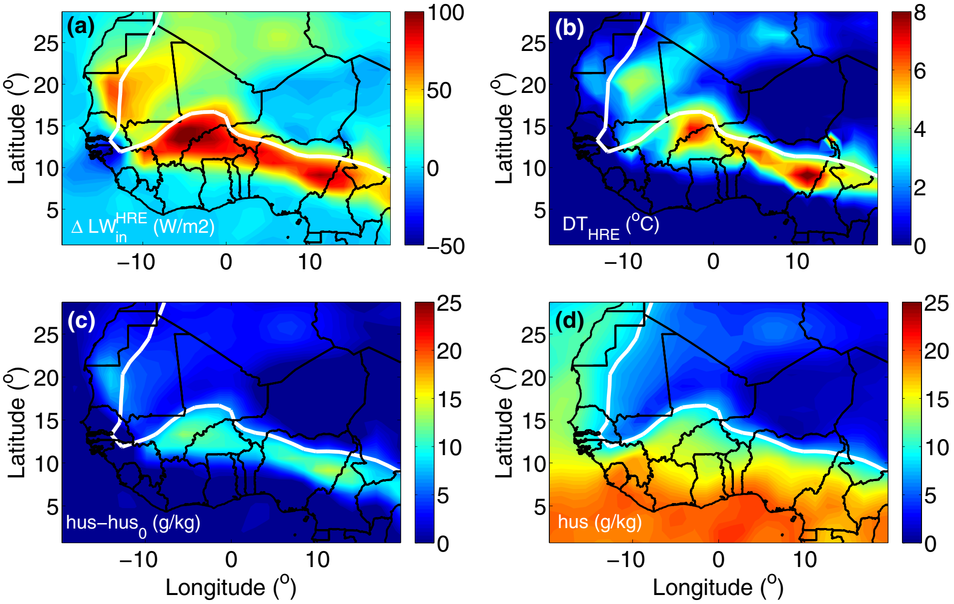

Fig. 14 ΔLW_{in}^{HRE} (**a**), ΔT_{HRE} (**b**), $hus - hus_0$ (**c**), hus (**d**) given by SARAWI on 15 April 2010, ie DOY 105 (see text for definitions). White line: ITD, defined with $hus = 8$ g/kg

between specific humidity on 15 April 2010 and the constant specific humidity field prescribed in the constant moisture simulation (Fig. 14c). The location of the ITD (here defined as the line of constant hus equal to 8 g/kg) is indicated with the white line.

ΔLW_{in}^{HRE} reaches strong values, up to 100 W/m^2 south of the ITD, leading to ΔT_{HRE} up to 13 °C. In Fig. 14, this strong HRE warming south of the ITD is associated with the northward progression of the monsoon flow in the previous days, and accounts for a specific humidity increase of about 10 g/kg (Fig. 14c).

Over the Sahara and other areas north of the ITD, the high values of ΔLW_{in}^{HRE} and ΔT_{HRE} are associated with the tropical plume, which also enhances low-level humidity and reaches about 5 °C (Fig. 14c, d).

Figure 14 also underlines that the western Sahel (west to 0° E) is more affected by HRE than the eastern Sahel (east to 0° E), consistently with an ITD that does not reach eastern Sahel in April 2010 (Fig. 14d). The processes affecting the western and eastern Sahel are therefore distinct, which partly explains why T_{min} were lower in Eastern Sahel (Fig. 7). However, HRE affects Nigeria and areas located to the east of 0° E but south of 12° N, which could also partly explains why T_{min} are high in this area (Fig. 7g, h).

6.5 Can we explain the observed LW_{in} anomalies with the SARAWI HRE estimate?

On average over the Sahel and Sahara, ΔLW_{in}^{HRE} reaches high values. Since HRE is caused by moisture which is anomalously high in April 2010 over the Sahel and Sahara (Fig. 6e,f), here we analyze whether the observed anomalies of LW_{in} that were explained neither by CRE nor ARE anomalies (Sect. 4) can be better explained by HRE.

The HRE longwave anomaly HRE^{ano} is computed by assuming that the LW_{in} climatological anomaly on DOY 91 (1 April 2010) is the sum of the longwave CRE, ARE and HRE anomalies. Then, we compute $HRE^{ano} = \Delta LW_{in}^{HRE} + HRE_0^{ano}$, with HRE_0^{ano} being the HRE anomaly on 1 April.

Figure 15 shows the April 2010 time series of longwave HRE^{ano} anomalies (light blue), together with the LW_{in} anomalies (black), longwave CRE (blue) and longwave ARE anomalies (red) observed with CERES, as well as the sum of the longwave anomalies CRE+ARE+HRE (orange), averaged over three areas: the Sahara (a), the western Sahel (b) and the eastern Sahel (c).

First, the order of magnitude of HRE^{ano} successfully matches that of the LW_{in} anomalies, particularly over the Sahara and the western Sahel. Secondly, when SARAWI estimates of HRE anomalies are added with CRE and ARE anomalies from CERES (orange curves), the resulting time series follows rather closely the observed LW_{in} anomalies (black), over the Sahara and the western Sahel.

This result suggests that in the Sahara, the strong positive anomaly of LW_{in}, which was not related to cloud or aerosol anomalies between DOY 100 and 120 is largely explained by the evolution of the HRE induced by the low-level advection of humidity operated by the tropical plume event (Fig. 15a). In the western Sahel (Fig. 15b), this HRE also explains a

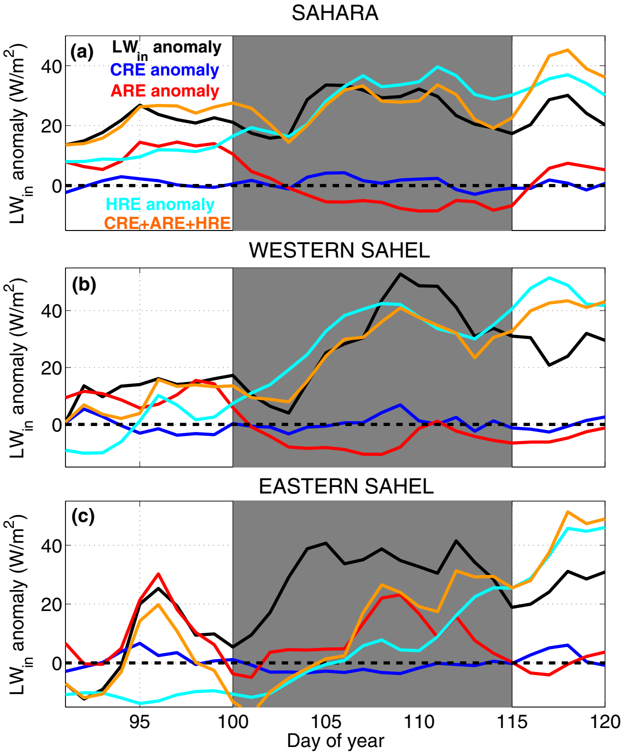

Fig. 15 April 2010 time series of anomalies of: LW_{in} (black), longwave CRE (blue), longwawe ARE (red) observed by CERES, longwave HRE computed by SARAWI (light blue) longwave CRE+ARE+HRE (orange); averaged over the Sahara (**a**), the western Sahel (west to 0°, **b**), the eastern Sahel (east to 0°, **c**)

major part of the observed anomaly, and is related to a northward penetration of the monsoon flow.

In the eastern Sahel, which is more affected by aerosols due to a strong dust episode after DOY 105, HRE remains weaker before DOY 105 (Fig. 15c). It increases later, when the ITD migrates northward in the eastern Sahel, and can explain the increase of LW_{in} anomalies in late April. However, in this area, the high anomaly of LW_{in} between DOY 100 and 107 is neither explained by clouds or aerosols nor by humidity radiative effects, which suggests the possible influence of other physical processes (complex radiative interactions that arise from overlapping between different types of aerosols and clouds; radiative influence of other greenhouse gases,...). In addition, the low number of in-situ observations assimilated in the reanalysis over Eastern Sahel may also play some role.

7 Discussion and conclusion

North Africa experienced a major heatwave in April 2010. The present study investigated physical processes acting during this event, using high frequency ground data (AMMA-CATCH), long-term gridded daily temperatures (BEST), satellite-based observations (CERES), climate model simulations (CNRM-AM), and a new soil-surface air layer prognostic model (SARAWI).

During spring 2010, very high daily minimum and maximum temperatures were observed North of 14° N, over large parts of the Sahel and Sahara, together with strong positive anomalies of LW_{in} and negative anomalies of SW_{in} at the surface, as well as strong positive anomalies of AOD, cloud cover and PW. The cloud cover and PW anomalies are associated with two distinct synoptic events (a tropical plume that reached the northern Sahara and a northward penetration of the monsoon flow in western Sahel), while the strong AOD anomaly that prevails during this period is centered on central Sahel.

The heatwave (identified with the methodology of Barbier et al. (2018)) lasts from 10 to 25 April 2010 and is particularly severe at night. Strong positive correlations are found between PW, T_{min} and LW_{in}, both in space and time, in the areas affected by the heatwave.

Satellite estimates show that, during the heatwave, Aerosol Radiative Effects (ARE) are stronger than Cloud Radiative Effects (CRE) by about + 30 W/m^2 for SW_{in}, and + 15 W/m^2 for LW_{in} over both the Sahel and the Sahara. The strong negative anomaly of SW_{in} is almost entirely explained by CRE over the Sahara, while it involves a combination of both CRE and ARE, over the Sahel. In contrast, the strong positive anomaly of LW_{in} (about + 30 W/m^2 over both the Sahara and Sahel) is much higher than longwave CRE or ARE anomalies, which means that neither the cloud cover nor the AOD can explain the observed anomalies of incoming longwave fluxes. The strong correlation between observed LW_{in} and PW anomalies points to the significance of a Humidity Radiative Effect (HRE), and this question is further explored with a climate model and a conceptual soil-atmospheric surface layer model.

In order to capture the chronology of the heatwave (and thus helps in performing relevant quantitative comparisons with observations, down to sub-daily time scales, Diallo et al. 2017), the dynamics of the climate-model simulation is nudged towards the ERA-interim meteorological reanalysis. We show that the CNRM-AM simulation faithfully reproduces the Saharan tropical plume event and the Sahelian monsoon surge, as well as the spatial patterns of surface incoming fluxes and temperatures observed during the heatwave. It exhibits systematic biases though, such as too low LW_{in}, LW_{net} and T_{min}. Those shortcomings do not affect the ability of the model to represent the sharp transition between the pre-heatwave and heatwave regime, closely associated with the arrival of the monsoon flow in the Sahel, whose main observed characteristics are well-reproduced. The pre-heatwave regime is dry with low nighttime temperatures, low LW_{in} and LW_{net} fluxes, and high Diurnal Temperature Range (DTR); while the heatwave regime is moister with higher nighttime temperatures, stronger LW_{in} and weaker DTR, both in observations and simulations.

In the CNRM-AM simulation, the nocturnal cooling of the atmospheric surface layer is almost entirely due to longwave radiative transfer, whereas daytime evolution of the surface-layer air temperature results mainly from the combination of two dominant processes: longwave radiation and turbulence. During the heatwave, nighttime air cooling by longwave radiation is lower. Similarly, the nighttime soil cooling is lower, because LW_{in} increases more than LW_{up}. The combination results in a stronger thermal coupling between the soil and the atmospheric surface layer. The increase of LW_{in} is strongly correlated with the increase in humidity on areas where the monsoon flow (Western Sahel) or the tropical plume (Sahara) moistens the environment.

The new conceptual model SARAWI (cf. Sect. 2.5) is used to explore further the radiative greenhouse effect of water vapor. We show that, at first order, regional-scale processes can be decoupled from local physics, namely turbulence and longwave radiative transfer between the soil and the atmospheric surface layer. By prescribing the former (here from the CNRM-AM simulation) and explicitly and pronostically computing the impact of the latter on temperatures, we are able to reproduce with a very good accuracy the surface energy budget, the radiative and turbulent warming of the atmospheric surface layer, LW_{in} fluxes, soil and air temperatures, and their diurnal cycles given by CNRM-AM. Unlike a complex 3D GCM, SARAWI is well-suited to perform and interpret sensitivity tests in simple and unambiguous ways. In the present study, it allows us to highlight the crucial impact of water vapor during the heatwave. Over the Sahel, the greenhouse effect of water vapor enhances LW_{in} and T_{min} up to 100 W/m^2 and 13 °C respectively.

In addition, a quantitative analysis shows that the sum of the HRE anomaly estimated using SARAWI, with the weaker CRE and ARE anomalies from CERES, explain the evolution of the observed LW_{in} anomaly over the Sahara and the western Sahel. This demonstrates that the increase of air emissivity due to the increase of moisture is the dominant driver of the heatwave nighttime temperatures; and that the severity of this heatwave can be explained by the increased greenhouse effect of water vapor.

In summary, our study provides insights into the interactions arising between processes operating at different scales: during the April 2010 heatwave, the synoptic-scale advection of warm air is negligible. However, the synoptic-scale advection of water vapor (associated with either the monsoon flow or the tropical plume) emerges as a fundamental driver. Indeed, the evolution of surface fluxes, soil and surface air temperatures are almost entirely explained by physical processes, among which longwave radiative transfers, which are very sensitive to water vapor variations.

Beyond this particular case study, a simplified model such as SARAWI can be useful for carrying sensitivity experiments at very low computation cost; e.g. for the implementation of new physical parameterizations. More broadly, such a modeling approach could also be useful for comparing the physical mechanisms operating in different climate models. This may be particularly relevant here given the importance of physical processes involved in land-atmosphere interactions on the climate during this period of the year.

Finally, this study further raises several open questions:

- Physical processes and mechanisms driving nighttime temperatures have been highlighted, but the evolution of T_{max} during this heatwave appeared complex, and seems to imply a balance between physical processes. To what extent do cloud, aerosol or humidity shortwave radiative effects lower T_{max}? To what extent can a heat accumulation phenomenon in the upper boundary-layer as described by Miralles et al. (2014) warm the low-layers during daytime via the afternoon convective and turbulent mixing?
- Could other processes involving larger-scale circulations, as recently highlighted in mid-latitudes by Zschenderlein et al. (2019) play a role? In particular for the Sahel, to what extend and how are tropical waves influencing Sahelian heatwave occurrence and characteristics? At relatively smaller scale, are convectively generated cold pools (which can advect water vapor up to the Sahara, (Garcia-Carreras et al. 2013)) playing a role during spring sahelian heatwaves?
- Barbier et al. (2018) show that there is a strong climatologic nighttime warming trend during heatwaves. To what extent can this trend be related to a climatic increase of atmospheric water vapor content (IPCC 2013), especially over the Saharan region (Evan et al. 2015) ? And how would this affect wet-bulb temperature which stands as an important variable with respect to heath considerations (e.g. Sherwood and Huber 2010)?
- Finally, can this link between water vapor and T_{min} help to analyze climate projections and reduce uncertainties on extreme weather frequency and severity for the coming century?

Acknowledgements This work has been done in the framework of the ACASIS project from the French national research agency (ANR). The authors acknowledge support from ANR ACASIS, grant ANR-13-487 SENV-0007 and from the AMMA-2050 project (grant number NE/M020428/1). Authors also acknowledge NASA for the dissemination of the CERES satellite products through the website https://ceres.larc.

nasa.gov/, the Berkeley Earth for their open global temperature database (berkeleyearth.org/), and the scientists and technicians who collected the AMMA-CATCH data in the Sahel. They also thank Mireille Tomasini for usefull discussions on heat budget analysis, and Clara Theeten for her careful proofreadings of the present paper.

Appendix: Configuration of the SARAWI simulations and tuned coefficients

In the SARAWI simulations used in the present study, physiographic and physical parameters are statistically tuned using the monthly-average values resolved by CNRM-AM. We also differentiate nighttime and daytime conditions when the considered parameter physically depends on static stability. This leads to:

ϵ_a: Coefficients a_i of Eq. 9 are estimated using longwave fluxes simulated by CNRM-AM which are regressed with the atmospheric specific humidity and air temperature. We can consider a_i coefficients obtained from a regression that include all points in North Africa, or alternatively use a_i coefficients which vary depending on the climate zone (Sahara, Sahel, Guinea). Both approaches lead to similar results (with a 5.3 W/m^2 or 1.3% uncertainty on LW_{in} and a 0.28 °C uncertainty on T_{2m}). A regional fitting over North Africa gives $a_1 = 0.667$, $a_2 = 1.17 \times 10^{-2}$ with *hus* in g/kg and $a_3 = 4.55 \times 10^{-4}$ with T_a in °C.

ϵ_s: As for ϵ_a, we use CNRM-AM longwave fluxes to estimate ϵ_s (which uses the ECOCLIMAP database, Champeaux et al. 2005; Faroux et al. 2013). It is almost constant and equal to 0.9946 ± 0.0065 over all North Africa in CNRM-AM. We take this mean-value as a constant for all continental grid points (this leads to a 0.11 W/m^2 or 0.03% uncertainty on LW_{in} and a 0.08 °C uncertainty on T_{2m} as compared to the local value for each grid point).

C_s: In order to correctly fit C_s, we use Eq. (2) with the resolved fluxes and temperatures given by CNRM-AM, which takes its soil physiographic characteristics from the ECOCLIMAP database (Champeaux et al. 2005; Faroux et al. 2013). We average the different terms for each grid point separately over daytime and nighttime, from which we estimate two physiographic 2D fields $C_s^{night}(lon, lat)$ and $C_s^{day}(lon, lat)$.

h_{rad}: We compute $h_{rad} = c_{rad}.\delta z$ at each grid point by determining the value of h_{rad} that minimizes the root mean square error between the CNRM-AM values of $\frac{\partial T_a}{\partial t}_{rlw}$ and the estimated values of that tendency according to Eq. (6). Results show that the value of c_{rad} is very homogeneous over all continental North Africa, so we choose to keep one constant value in SARAWI equal to the average over the continental area: $h_{rad} = 4.74.\delta z$. Physically, h_{rad} corresponds to a characteristic penetration depth of the upwelling longwave flux emitted by the surface, or alternatively to the depth of the layer radiatively warmed (or cooled) by the surface.

h_{turb}: It is fixed equal to the height between the first and the second layers of the CNRM-AM simulation (35 m).

c_{t2m}: The parameterization available in CNRM-AM (Mahfouf et al. 1995) is used here to prescribe c_{t2m}, in order to facilitate comparison with the diagnosed T_{2m} in CNRM-AM simulation.

C_h, K_s, K_h: In coupled soil-atmospheric models, the drag coefficient C_h usually depends on the static stability (see Noilhan and Mahfouf 1996 for the ISBA model used in CNRM-AM). Similarly, the turbulent diffusivity in the low layers also strongly varies with the static stability (e.g. Yasuda 1988; Largeron et al. 2010).

Here, we choose to use constant daytime values: $C_h = 4.10^{-3}$, $K_s = 1.6 \times 10^{-4}$, $K_h = 0.94\ \mathrm{m}^2 \cdot \mathrm{s}^{-1}$; and constant nighttime values about 8 times lower: $C_h = 5 \times 10^{-4}$, $K_s = 2 \times 10^{-5}$, $K_h = 0.08\ \mathrm{m}^2 \cdot \mathrm{s}^{-1}$. Values are tuned to recover the heat fluxes given by the CNRM-AM simulation.

References

Balkanski Y, Schulz M, Claquin T, Guibert S (2007) Reevaluation of mineral aerosol radiative forcings suggests a better agreement with satellite and aeronet data. Atmos Chem Phys 7(1):81–95

Barbier J, Guichard F, Bouniol D, Couvreux F, Roehrig R (2018) Detection of intraseasonal large-scale heat waves: characteristics and historical trends during the Sahelian spring. J Clim 31(1):61–80

Basart S, Pérez García-Pando C, Cuevas E, Baldasano Recio JM, Gobbi P (2009) Aerosol characterization in Northern Africa, Northeastern Atlantic, Mediterranean Basin and Middle East from direct-sun aeronet observations. Atmos Chem Phys 9(21):8265–8282

Baup F, Mougin E, De Rosnay P, Timouk F, Chênerie I (2007) Surface soil moisture estimation over the AMMA Sahelian site in Mali using ENVISAT/ASAR data. Remote Sens Environ 109(4):473–481

Beniston M (2004) The 2003 heat wave in Europe: a shape of things to come? An analysis based on Swiss climatological data and model simulations. Geophys Res Lett 31(2)

Black E, Blackburn M, Harrison G, Hoskins B, Methven J (2004) Factors contributing to the summer 2003 European heatwave. Weather 59(8):217–223

Bouniol D, Couvreux F, Kamsu-Tamo P-H, Leplay M, Guichard F, Favot F, O'Connor EJ (2012) Diurnal and seasonal cycles of cloud occurrences, types, and radiative impact over West Africa. J Appl Meteorol Climatol 51(3):534–553

Brooks N, Legrand M (2000) Dust variability over Northern Africa and rainfall in the Sahel. In: Linking climate change to land surface change. Springer, Berlin, pp 1–25

Champeaux J, Masson V, Chauvin F (2005) Ecoclimap: a global database of land surface parameters at 1 km resolution. Meteorol Appl 12(1):29–32

Coindreau O, Hourdin F, Haeffelin M, Mathieu A, Rio C (2007) Assessment of physical parameterizations using a global climate model with stretchable grid and nudging. Mon Weather Rev 135(4):1474–1489

Couvreux F, Guichard F, Bock O, Campistron B, Lafore J-P, Redelsperger J-L (2010) Synoptic variability of the monsoon flux over West Africa prior to the onset. Q J R Meteorol Soc 136(S1):159–173

Cuxart J, Bougeault P, Redelsperger J-L (2000) A turbulence scheme allowing for mesoscale and large-eddy simulations. Q J R Meteorol Soc 126(562):1–30

Decharme B, Martin E, Faroux S (2013) Reconciling soil thermal and hydrological lower boundary conditions in land surface models. J Geophys Res Atmos 118(14):7819–7834

Decharme B, Brun E, Boone A, Delire C, Le Moigne P, Morin S (2016) Impacts of snow and organic soils parameterization on Northern Eurasian soil temperature profiles simulated by the ISBA land surface model. Cryosphere 10(2):853–877

Dee D, Uppala S, Simmons A, Berrisford P, Poli P, Kobayashi S, Andrae U, Balmaseda M, Balsamo G, Bauer P et al (2011) The era-interim reanalysis: configuration and performance of the data assimilation system. Q J R Meteorol Soc 137(656):553–597

Deme A, Gaye AT, Hourdin F (2017) Climate projections in West Africa: the obvious and the uncertain. In: Sultan B, R Lalou R, Sanni MA, Oumarou A, Soumaré MA (eds) Rural societies in the face of climatic and environmental changes in West Africa, IRD Editions. AN13: 9782709924245 and 9782709924269

Déqué M, Dreveton C, Braun A, Cariolle D (1994) The arpege/ifs atmosphere model: a contribution to the French community climate modelling. Clim Dyn 10(4–5):249–266

Diallo FB, Hourdin F, Rio C, Traore A-K, Mellul L, Guichard F, Kergoat L (2017) The surface energy budget computed at the grid-scale of a climate model challenged by station data in West Africa. J Adv Model Earth Syst 9(7):2710–2738

Doelling DR, Loeb NG, Keyes DF, Nordeen ML, Morstad D, Nguyen C, Wielicki BA, Young DF, Sun M (2013) Geostationary enhanced temporal interpolation for CERES flux products. J Atmos Ocean Technol 30(6):1072–1090

Evan AT, Flamant C, Lavaysse C, Kocha C, Saci A (2015) Water vapor-forced greenhouse warming over the Sahara Desert and the recent recovery from the Sahelian drought. J Clim 28(1):108–123

Faroux S, Kaptué Tchuenté A, Roujean J-L, Masson V, Martin E, Moigne PL (2013) ECOCLIMAP-II/Europe: a twofold database of ecosystems and surface parameters at 1 km resolution based on satellite information for use in land surface, meteorological and climate models. Geosci Model Dev 6(2):563–582

Fischer EM (2014) Climate science: autopsy of two mega-heatwaves. Nat Geosci 7(5):332–333

Fontaine B, Janicot S, Monerie P-A (2013) Recent changes in air temperature, heat waves occurrences, and atmospheric circulation in Northern Africa. J Geophys Res Atmos 118(15):8536–8552

Fouquart Y, Bonnel B (1980) Computations of solar heating of the earth's atmosphere—a new parameterization. Beitr Phys Atmos 53:35–62

Fröhlich L, Knippertz P, Fink AH, Hohberger E (2013) An objective climatology of tropical plumes. J Clim 26(14):5044–5060

Fu Q, Liou K (1992) On the correlated k-distribution method for radiative transfer in nonhomogeneous atmospheres. J Atmos Sci 49(22):2139–2156

Garcia-Carreras L, Marsham J, Parker D, Bain C, Milton S, Saci A, Salah-Ferroudj M, Ouchene B, Washington R (2013) The impact of convective cold pool outflows on model biases in the Sahara. Geophys Res Lett 40(8):1647–1652

Guérémy J (2011) A continuous buoyancy based convection scheme: one-and three-dimensional validation. Tellus A 63(4):687–706

Guichard F, Kergoat L, Mougin E, Timouk F, Baup F, Hiernaux P, Lavenu F (2009) Surface thermodynamics and radiative budget in the Sahelian Gourma: seasonal and diurnal cycles. J Hydrol 375(1):161–177

Guichard F, Kergoat L, Mougin E, Hourdin F (2012) The annual cycle of temperature in the Sahel and its climatic sensitivity. In: AGU Fall Meeting Abstracts, vol 1, p 1004

Guichard F, Kergoat L, Hourdin F, Léauthaud C, Barbier J, Mougin E, Diarra B (2017) Climate warming observed in the Sahel since 1950. In: Sultan B, Lalou R, Sanni MA, Oumarou A, Soumaré MA (eds) Rural societies in the face of climatic and environmental changes in West Africa. AN13: 9782709924245 and 9782709924269

Herrero J, Polo M (2012) Parameterization of atmospheric longwave emissivity in a mountainous site for all sky conditions. Hydrol Earth Syst Sci 16(9):3139–3147

Honda Y, Kondo M, McGregor G, Kim H, Guo Y-L, Hijioka Y, Yoshikawa M, Oka K, Takano S, Hales S et al (2014) Heat-related mortality risk model for climate change impact projection. Environ Health Prev Med 19(1):56–63

Hourdin F, Gueye M, Diallo B, Dufresne J-L, Escribano J, Menut L, Marticoréna B, Siour G, Guichard F (2015) Parameterization of convective transport in the boundary layer and its impact on the representation of the diurnal cycle of wind and dust emissions. Atmos Chem Phys 15(12):6775–6788

IPCC (2013) Climate change 2013: the physical science basis: Working Group I contribution to the Fifth assessment report of the Intergovernmental Panel on Climate Change. Cambridge University Press, Cambridge

IPCC (2014) Climate Change 2014—impacts adaptation and vulnerability: regional aspects. Cambridge University Press, Cambridge

Klose M, Shao Y, Karremann MK, Fink AH (2010) Sahel dust zone and synoptic background. Geophys Res Lett 37(9)

Knippertz P, Martin JE (2005) Tropical plumes and extreme precipitation in subtropical and tropical West Africa. Q J R Meteorol Soc 131(610):2337–2365

Largeron Y, Staquet C, Chemel C (2010) Turbulent mixing in a katabatic wind under stable conditions. Meteorol Z 19(5):467–480

Leroux S, Bellon G, Roehrig R, Caian M, Klingaman NP, Lafore J-P, Musat I, Rio C, Tyteca S (2016) Inter-model comparison of subseasonal tropical variability in aquaplanet experiments: effect of a warm pool. J Adv Model Earth Syst

Lohou F, Kergoat L, Guichard F, Boone A, Cappelaere B, Cohard J-M, Demarty J, Galle S, Grippa M, Peugeot C et al (2014) Surface response to rain events throughout the West African monsoon. Atmos Chem Phys 14(8):3883–3898

Lopez P (2002) Implementation and validation of a new prognostic large-scale cloud and precipitation scheme for climate and data-assimilation purposes. Q J R Meteorol Soc 128(579):229–257

Mahfouf J, Manzi A, Noilhan J, Giordani H, Déqué M (1995) The land surface scheme ISBA within the Météo-France climate model arpege. Part I. Implementation and preliminary results. J Clim 8(8):2039–2057

Marsham JH, Parker DJ, Todd MC, Banks JR, Brindley HE, Garcia-Carreras L, Roberts AJ, Ryder CL (2016) The contrasting roles of water and dust in controlling daily variations in radiative heating of the summertime Saharan heat low. Atmos Chem Phys 16(5):3563–3575

Martin G, Peyrillé P, Roehrig R, Rio C, Caian M, Bellon G, Codron F, Lafore J-P, Poan D, Idelkadi A (2017) Understanding the West African monsoon from the analysis of diabatic heating distributions as simulated by climate models. J Adv Model Earth Syst 9(1):239–270

Masson V, Champeaux J-L, Chauvin F, Meriguet C, Lacaze R (2003) A global database of land surface parameters at 1-km resolution in meteorological and climate models. J Clim 16(9):1261–1282

Masson V, Le Moigne P, Martin E, Faroux S, Alias A, Alkama R, Belamari S, Barbu A, Boone A, Bouyssel F et al (2013) The SURFEXv7. 2 land and ocean surface platform for coupled or offline simulation of earth surface variables and fluxes. Geosci Model Dev 6:929–960

Mellor GL, Yamada T (1982) Development of a turbulence closure model for geophysical fluid problems. Rev Geophys 20(4):851–875

Michou M, Nabat P, Saint-Martin D (2015) Development and basic evaluation of a prognostic aerosol scheme (v1) in the CNRM climate model CNRM-CM6. Geosci Model Dev 8(3)

Miralles DG, Teuling AJ, Van Heerwaarden CC, de Arellano JV-G (2014) Mega-heatwave temperatures due to combined soil desiccation and atmospheric heat accumulation. Nat Geosci 7(5):345–349

Mlawer EJ, Taubman SJ, Brown PD, Iacono MJ, Clough SA (1997) Radiative transfer for inhomogeneous atmospheres: RRTM, a validated correlated-k model for the longwave. J Geophys Res Atmos 102(D14):16663–16682

Moron V, Oueslati B, Pohl B, Rome S, Janicot S (2016) Trends of mean temperatures and warm extremes in Northern Tropical Africa (1961–2014) from observed and PPCA-reconstructed time series. J Geophys Res Atmos 121(10):5298–5319

Mougin E, Hiernaux P, Kergoat L, Grippa M, De Rosnay P, Timouk F, Le Dantec V, Demarez V, Lavenu F, Arjounin M et al (2009) The AMMA-CATCH Gourma observatory site in Mali: relating climatic variations to changes in vegetation, surface hydrology, fluxes and natural resources. J Hydrol 375(1):14–33

Nabat P, Somot S, Mallet M, Chiapello I, Morcrette J, Solmon F, Szopa S, Dulac F, Collins W, Ghan S et al (2013) A 4-D climatology (1979–2009) of the monthly tropospheric aerosol optical depth distribution over the Mediterranean region from a comparative evaluation and blending of remote sensing and model products. Atmos Meas Tech 6(5):1287

Noilhan J, Mahfouf J-F (1996) The isba land surface parameterisation scheme. Glob Planet Change 13(1–4):145–159

Noilhan J, Planton S (1989) A simple parameterization of land surface processes for meteorological models. Mon Weather Rev 117(3):536–549

Perkins SE (2015) A review on the scientific understanding of heatwaves—their measurement, driving mechanisms, and changes at the global scale. Atmos Res 164:242–267

Piriou J-M, Redelsperger J-L, Geleyn J-F, Lafore J-P, Guichard F (2007) An approach for convective parameterization with memory: separating microphysics and transport in grid-scale equations. J Atmos Sci 64(11):4127–4139

Prata A (1996) A new long-wave formula for estimating downward clear-sky radiation at the surface. Q J R Meteorol Soc 122(533):1127–1151

Ramanathan V, Cess R, Harrison E, Minnis P, Barkstrom B et al (1989) Cloud-radiative forcing and climate: results from the earth radiation budget experiment. Science 243(4887):57

Ricard J, Royer J-F (1993) A statistical cloud scheme for use in an AGCM. Ann Geophys 11:1095–1115

Roehrig R, Bouniol D, Guichard F, Hourdin F, Redelsperger J-L (2013) The present and future of the west african monsoon: a process-oriented assessment of CMIP5 simulations along the AMMA transect. J Clim 26(17):6471–6505

Rohde R, Muller R, Jacobsen R, Perlmutter S, Rosenfeld A, Wurtele J, Curry J, Wickhams C, Mosher S (2013) Berkeley earth temperature averaging process. Geoinf Geostat 1:2

Rutan DA, Kato S, Doelling DR, Rose FG, Nguyen LT, Caldwell TE, Loeb NG (2015) Ceres synoptic product: methodology and validation of surface radiant flux. J Atmos Ocean Technol 32(6):1121–1143

Sane Y, Bonazzola M, Rio C, Chambon P, Fiolleau T, Musat I, Hourdin F, Roca R, Grandpeix J-Y, Diedhiou A (2012) An analysis of the diurnal cycle of precipitation over Dakar using local rain-gauge data and a general circulation model. Q J R Meteorol Soc 138(669):2182–2195

Sherwood SC, Huber M (2010) An adaptability limit to climate change due to heat stress. Proc Natl Acad Sci 107(21):9552–9555

Stephens GL, Wild M, Stackhouse PWJ, L'Ecuyer T, Kato S, Henderson DS (2012) The global character of the flux of downward longwave radiation. J Clim 25(7):2329–2340

Sultan B, Gaetani M (2016) Agriculture in West Africa in the twenty-first century: climate change and impacts scenarios, and potential for adaptation. Front Plant Sci 7

Timouk F, Kergoat L, Mougin E, Lloyd C, Ceschia E, Cohard J-M, De Rosnay P, Hiernaux P, Demarez V, Taylor C (2009) Response of surface energy balance to water regime and vegetation development in a Sahelian landscape. J Hydrol 375(1):178–189

Voldoire A, Sanchez-Gomez E, y Mélia DS, Decharme B, Cassou C, Sénési S, Valcke S, Beau I, Alias A, Chevallier M et al (2013) The CNRM-CM5. 1 Global climate model: description and basic evaluation. Clim Dyn 40(9–10):2091–2121

Wielicki BA, Barkstrom BR, Harrison EF, Lee RB III, Louis Smith G, Cooper JE (1996) Clouds and the earth's radiant energy system (CERES): an earth observing system experiment. Bull Am Meteorol Soc 77(5):853–868

Wielicki BA, Barkstrom BR, Baum BA, Charlock TP, Green RN, Kratz DP, Lee RB, Minnis P, Smith GL, Wong T et al (1998) Clouds and the earth's radiant energy system (CERES): algorithm overview. IEEE Trans Geosci Remote Sens 36(4):1127–1141

Yasuda N (1988) Turbulent diffusivity and diurnal variations in the atmospheric boundary layer. Bound Layer Meteorol 43(3):209–221

Zschenderlein P, Fink AH, Pfahl S, Wernli H (2019) Processes determining heat waves across different European climates. Q J R Meteorol Soc